IMPROVED TEMPORAL AND SPATIAL FOCUSING USING DECONVOLUTION: THEORETICAL, NUMERICAL AND EXPERIMENTAL STUDIES

by

Johannes Douma

A thesis submitted to the Faculty and the Board of Trustees of the Colorado School of Mines in partial fulfillment of the requirements for the degree of Master of Science (Geophysics).

Golden, Colorado

Date _____

Signed: _____
Johannes Douma

Signed: _____
Dr. Roel Snieder
Thesis Advisor

Golden, Colorado

Date _____

Signed: _____
Dr. Terry Young
Professor and Head
Department of Geophysics

ABSTRACT

Time Reversal can be used to time reverse and propagate the measured scattered waveforms to a point in both time and space, ideally to a delta function $\delta(\vec{r})\delta(t)$. This is commonly referred to as time reversal focusing and has led to time reversal being applied in a wide variety of fields such as medicine, communications, nondestructive evaluation (NDE), and seismology.

In practice, time reversal is not optimal for generating a delta function focus if certain conditions are not upheld. For time reversal to work perfectly, the following four conditions must be present: (1) one must record for an infinitely long period of time; (2) Green's functions must be assumed to contain infinite bandwidth; (3) attenuation must be absent within the medium; and (4) one must have full coverage of the wavefield. Due to the need for these conditions, much research is being carried out in order to enhance the time reversal process in practice.

We introduce deconvolution, a simple and robust approach, in order to calculate an optimal signal for back propagation designed to give an improved focus. We demonstrate experimentally that deconvolution is able to dramatically improve the temporal focus compared to time reversal. Through a joint project with Los Alamos National Laboratory, we compared time reversal to deconvolution. The results showed that deconvolution was able to dramatically improve the temporal focus for a source and a receiver which were both located on the surface of our object. We then continued our experimental studies of deconvolution by doing a joint project with researcher Dr. Ernst Niederleithinger from the Federal Institute for Materials Research and Testing (BAM). For this experiment, we placed multiple sources within a concrete block and recorded the source wavefields on the surface with a single receiver. This experiment was designed to further test the robust nature of deconvolution and compare its temporal focusing capability to that of time reversal. All of these experimental

studies show that deconvolution was able to improve the temporal focus compared to time reversal.

We continued our comparison study between time reversal and deconvolution and demonstrated theoretically, experimentally, and numerically that deconvolution also improves spatial focusing. We give a proof explaining why one would expect improved spatial focusing when there is improved temporal focusing for both a acoustic and elastic media. We then demonstrate in our experiments the improved spatial focus achieved using deconvolution by scanning around the source location with a laser vibrometer at the time of focus for an acoustic case. Finally, we use deconvolution to locate synthetic microseismic events to prove numerically that improved temporal focusing leads to improved spatial focusing for both acoustic and elastic media.

TABLE OF CONTENTS

LIST OF FIGURES

LIST OF SYMBOLS

waterlevel parameter . . . . . γ

regularization term . . . . . ϵ

convolution . . . . . $\star$

complex conjugate . . . . . *

LIST OF ABBREVIATIONS

Time Reversal . . . . . TR

Deconvolution . . . . . DC

ACKNOWLEDGMENTS

I would first like to specifically thank Dr. Roel Snieder. He has been an advisor to me in every aspect of my life. The lessons I have learned from him will never be forgotten and have truly changed the way I look at life. He was the perfect mentor for my research because he knew exactly how to push me further. He was there for me when I needed help but also pushed me away when he knew I could and should do it myself. Thank you for everything Dr. Roel Snieder.

I would also like to thank my parents, Jan and Ivonne Douma. Without their support, this thesis would have never been made possible. They assisted me in every way and were always there to help. It has been a tough 4 years to complete my Masters and Bachelors at the same time. However, I could always give them a call when I needed some words of encouragement. I want to thank my mom for always giving me advice on my personal life outside of work which is so important to be maintained. I would also like to deeply thank my father for all his advice during my studies and along my career moves. I will always be grateful for what they have done for me. Thanks for being the best parents!

This Master's thesis would not have been possible without the help and joint work with Dr. T.J. Ulrich and Dr. Brian Anderson from Los Alamos National Labratory and Dr. Ernst Niederleithinger from BAM.

I would also like to thank BAM (specifically F. Mielentz and R. Feldmann) for providing equipment and software for one of our experimental studies, and the civil engineering lab at CSM (M. Mooney, M. Gutierrez and L. Frash) for providing Dr. Ernst Niederleithinger and I with space and resources to make the concrete specimen and to carry out our experiment.

Finally, thank you to my friends and colleagues at CWP, Esteban Diaz Pantin, Ashley Fish, Detchai Ittharat, Farhad Bazargani, Satyan Singh, Francesco Perrone, my parents again, my "cousin" Huub Douma and "honorary Douma" Roel Snieder Douma.

CHAPTER 1

INTRODUCTION

1.1 Motivation

Several methods are used to evaluate acoustic signal; generated by events in media such as water, rocks, metals or concrete. Most of them are summarized as acoustic emission methods (AE), mainly travel time evaluation methods to localize the point of origin. Sophisticated methods have been developed in seismology to localize and characterize earthquakes. Time Reversal (TR) has been the focus of much research in acoustics due to its ability to compress the measured scattered waveforms back at the source point in both space and time [1–4].This has led to TR being applied in a wide variety of fields such as medicine, communication or nondestructive evaluation. However, continued work is being done to improve TR ability to focus energy.

Another field where time reversal has been the focus of much work is microseismic event locating. Due to hydraulic fracturing becoming a common practice for unconventional gas and oil fields, there has been an increased interest into the study of microseismic events. Clusters of microseismic events delineate faults and the formation of fractures, and can indicate new or reactivating regions of failure. These microseismic events can be generated naturally or as a result of hydraulic stimulation [5, 6]. Therefore, the petroleum industry desires to develop more accurate ways of locating, and monitoring microseismic events to potentially improve their relationship to production and completion data [7]. If one timereverses the waves at every point in space, the wavefield will focus onto the original source location. If, however, the wavefield is sampled at only a limited number of locations, then it is not obvious that time reversal is the optimal way to focus energy on the original source.

In this thesis, a technique is demonstrated to improve the temporal and spatial focusing achieved at a source location. The method uses deconvolution which is then applied to a wide

variety of experiments to study the robust nature and capabilities of deconvolution to improve the focusing at a source location. Additionally, we demonstrate the impact deconvolution may have upon improving the microseismic events locations in both an acoustic and elastic media. The proposed method is simple and proven to be robust. Additionally, its costs are negligible due to deconvolution being a simple preprocessing step to the recorded data.

1.2 Contribution

This thesis consists of published or submitted papers and abstracts. The following describes where each paper or abstract was submitted and my contribution towards each project.

Chapter 2 is submitted to the journal *Wave Motion*. The paper was a result of a joint project between Los Alamos National Laboratory and CWP and shows theoretical and experimental examples why improved temporal focusing leads to improved spatial focusing. Roel Snieder and I, from CWP, worked with T.J. Ulrich and Brian E. Anderson, from Los Alamos, to improve the temporal focus in an ultrasound experiment. I developed the method and implemented it into a code which could be used in the laboratory. T.J and Brian then conducted the experiments using the code. Afterwards, I analyzed the data and T.J. then wrote the final version of the paper; I was second author.

Chapter 3 represents an abstract published in *the German Society for Non-Destructive Testing(DGZfP) conference 2014*. This was a joint project between Dr. Ernst Niederleithinger from Federal Institute for Materials Research and Testing (BAM), Roel Snieder and me. The abstract demonstrates experimentally that deconvolution dramatically improves the temporal focus for a single source event within a medium. Dr. Ernst Niederleithinger and I created the specimen (a concrete block) and experimental set up. I then adjusted the code previously developed for Los Alamos to work for our experiment. Dr. Ernst Niederleithinger and I then carried out the experiments together in the lab. As first author, I was responsible for analyzing the data and writing the abstract.

Chapter 4 represents a paper to be submitted to *Journal of Non-destructive Evaluation*. This was a joint project between Dr. Ernst Niederleithinger from Federal Institute for Materials Research and Testing (BAM), Dr. Roel Snieder and me. The paper demonstrates theoretically and through multiple experiments the robust nature of deconvolution by investigation the effect of changing the stabilization constant used in the deconvolution and the impact multiple sources has upon deconvolutions' focusing abilities. The project was a continuation of our work shown in Chapter 3. We used the same specimen as explained in Chapter 3. I then adjusted the codes to run these new experimental studies. Ernst and I were then responsible for running the experiments in the lab. I was responsible for analyzing the data and writing the abstract.

Chapter 5 represents an abstract published in *Society of Exploration Geophysicists conference 2013*. I expanded Ashley Fish's thesis work by comparing time reversal to deconvolution for microseismic event locating. The abstract shows theoretically and numerically that deconvolution is able to improve the locating of microseismic events for an acoustic media. I generated the code for numerical modeling of this acoustic case. Dr. Roel Snieder and I, together developed the theory of why improved temporal focusing leads to improved spatial focusing. As first author, I took the responsibility of writing this abstract.

Chapter 6 is a paper submitted *Geophysical Journal International*, and consists of my joint work done with Dr. Roel Snieder. The paper demonstrates theoretically and numerically that deconvolution is able to improve the focusing of the elastic waves due to a microseismic source within a elastic medium. My responsibility was to develop a numerical model for elastic wave propagation using madagascar, implement a double-couple source code, apply deconvolution and time reversal to different types of sources (point force, double-couple), and analyze the data. Dr. Roel Snieder worked on the theory for the improved spatial focusing for the elastic case. He and I wrote different sections of the paper, and flipped a coin for first authorship. We both felt we had contributed equally to the work.

CHAPTER 2

IMPROVING SPATIO-TEMPORAL FOCUSING AND SOURCE RECONSTRUCTION THROUGH DECONVOLUTION

In this study, a technique is demonstrated to improve the ability of time reversal to both spatially and temporally focus, or compress, elastic wave energy, or to improve the quality of the reconstruction of the source signal. This method utilizes the deconvolution, or inverse filter, in single channel time reversal experiments in solids. Special attention is given to the necessary procedure for improving source signal reconstruction in real experimental conditions. It is also demonstrated theoretically and numerically that good temporal focusing implies that the radius in the spherically symmetric part of the spatial focus is small.

2.1 Introduction

Time Reversal (TR) in acoustics has been the focus of much research [1–4]. This has led to many applications in a wide variety of fields, such as medicine, communications, nondestructive evaluation (NDE), seismology, etc. In many of these applications, the ability to use TR depends upon its ability to precisely compress the measured scattered waveforms to a point in both time and space, ideally a delta function, $\delta(t)$, which is commonly referred to as TR focusing. The desire to enhance the TR process to focus wave energy has led researchers to develop a variety of ways to accomplish this. Some techniques use arrays of input transducers, measure the wave field with an array near the desired focal spot, and then optimize the spatial and temporal focusing [8–16]. Other methods use an array of input transducers and optimize the temporal focusing at an output transducer [17–21]. Some of these techniques require, or at least benefit greatly from, large arrays, while others may enhance temporal focusing at the expense of spatial localization.

Another aspect of the focal signal that is of interest for certain applications, i.e., seismology (source mechanics identification), communications, NDE, or anywhere else that the

focused signal fidelity is important, is the quality of the reconstruction of the source signal. As TR, in principle, recreates the source signal (in reverse, of course) interest has grown in this aspect of source recreation. In experimental TR studies, however, there is an inseparable transducer effect in this process. For this reason it would be desirable to find a method capable of removing this effect such that source reconstruction is enhanced.

We explore a simple approach and use deconvolution, a primitive, though robust, version of the inverse filter[8, 12], to provide an input signal to be used in the TR process. We then document what additional processing is necessary to either create an approximate delta function $\delta(t)$ (limited by available bandwidth) or a reconstruction of an arbitrary source function, $S(t)$, as an output at the focal point, and show laboratory ultrasound experiments that the temporal focusing thus obtained is superior to that obtained by using reciprocal time reversal. We also show the reconstruction of the source function, or a delta function as desired, is possible through the prescribed procedure. By scanning the sample near the focal point, we find that this improved temporal focusing is accompanied by a better spatial focusing. We then show theoretically that improved temporal focusing implies enhanced spatial focusing for the spherical average of the focus. The method described in this paper enhances both spatial and temporal focusing for a single channel and can be expanded to any number of channels. In contrast to many previous applications of the inverse filter[8, 9, 12], we also explore the effectiveness of using deconvolution for small time reversal mirrors (TRM), e.g., single channel[22, 23], in bounded media, with limited available bandwidth, and for the purpose of source reconstruction.

2.2 Deconvolution as an inverse filter

The time reversal process, a matched field process, is often used in an attempt to produce an impulsive focus, $\delta(t)$, of energy. This process utilizes a recorded impulse response, or Green function G_{AB} between two points A and B, a simple reversal in time of that signal and broadcast of it back into the same medium, from A to B or *vice versa*, to focus energy

at the appropriate point in space (A or B); or

$$\int_{-\infty}^{\infty} G_{AB}(\tau) G_{AB}(\tau - t) d\tau = \delta(t) \ , \tag{2.1}$$

where reciprocity has been used to replace the Green function G_{BA} with G_{AB}. Equation 2.1 states that the autocorrelation of $G_{AB}(t)$ is ideally equal to a delta function. In practice, actual TR experiments cannot recreate a true delta function focus as one or more conditions necessary to satisfy Eq. 2.1 are typically violated. For example, due to either time, physical memory, or attenuation constraints, it is not possible to record for an infinitely long period of time. Also, the Green functions here are assumed to contain a flat, infinite bandwidth, which is routinely not the case in experiments particularly when using narrowband response transducers such as piezoelectric types. For this reason we, as others before us, asked the question: what would be required to most closely approach an impulse-like TR focus given typical experimental limitations?

Going back to Eq. 2.1, we can rewrite this (using a convolution notation, rather than the integral form) as

$$F(t) = g(t) \star R(t) \approx \delta(t) \ , \tag{2.2}$$

where $F(t)$ is the focal signal or source reconstruction, $R(t)$ is the recorded signal measured at the receiver location B from the initial source propagation, and $g(t)$ is the signal necessary to be back propagated for focusing, also known as the result of the inverse filter (IF), as will become evident. Here we restrict ourselves to looking only at signals between the two points A and B and thus have removed them from the notation. We also change from a Green function notation so as not to imply that we necessarily have an infinite bandwidth available. Further, since we only employ a single channel, we cannot utilize the singular value decomposition step proposed by Tanter *et al.* for noise rejection[8], and thus we rely on a high signal to noise ratio. From Eq. 2.2, we aim to approximate the focal signal $F(t)$ to a delta function by assuming that the recorded impulse response $R(t)$ contains information enough to produce an IF signal $g(t)$ to broadcast in our TR focusing procedure.

Deconvolution equates to inverse filtering by transforming to the frequency domain, thus Eq. (2.2) becomes

$$F(\omega) = g(\omega)R(\omega) \approx 1 \ , \tag{2.3}$$

which can easily be manipulated to provide $g(\omega)$ simply from measuring $R(\omega)$ (or rather from the FFT of $R(t)$). As such, we can now calculate the IF signal which should produce the most impulse-like TR focus from

$$g(\omega) = \frac{1}{R(\omega)} = \frac{R^*(\omega)}{|R(\omega)|^2}. \tag{2.4}$$

where $*$ denotes a complex conjugate operation. This expression gives a mathematical expression for $g(\omega)$, but this may not be practical for experimental use in the event that there is a limited bandwidth, significant background noise, or more precisely if $R(\omega) = 0$ at any frequency. To avoid this we simply add a constant to the denominator to ensure that we never divide by 0, hence we replace Eq. 2.4 by

$$g(\omega) = \frac{R^*(\omega)}{|R(\omega)|^2 + \epsilon} \ , \tag{2.5}$$

where ϵ is a constant related to the original received signal as

$$\epsilon = \gamma \ \text{mean}(|R(\omega)|^2). \tag{2.6}$$

The quantity γ, which is sometimes referred to as the waterlevel parameter [24], is an arbitrary constant chosen to optimally reduce the effect of noise introduced through the IF procedure. Here we use $\gamma = 0.9$ for all experiments. The value 0.9 was chosen based on optimizing the focus energy in a process similar to that developed by Clayton *et al.*[24].

As the above derivation has been performed in the frequency domain, it is necessary to transform back to the time domain to recover the deconvolved signal, $g(t)$ to be used in the time reversal experiments. It is worth noting that this procedure produces a $g(t)$ that can be used directly for rebroadcasting, i.e., there is no need to perform a TR operation $g(t) \rightarrow g(-t)$ to obtain a focused signal. While this completes the deconvolution optimization procedure used in this paper, it is only a portion of the inverse filter procedure as defined by Tanter

et al.[8], and utilized most recently by Gallot *et al.*[12] For the full IF procedure a singular value decomposition (SVD) is often used for noise suppression, but since we are limited to a single channel in this study, SVD results in a simple normalization by a constant, and can thus be ignored. Thus the use of the deconvolution operation with a single channel requires a high signal to noise ratio.

From the above derivation it is easy to assume that the deconvolution is providing the best available signal for recreating a delta function. However, upon closer examination it is actually recreating a function related to the source function, which in previous studies of the inverse filter was designed, or assumed, to be impulse-like. If we separate the received signal into the Green function ($G(\omega)$) propagating the source function ($S(\omega)$) from A to B, the transducer responses at A and B ($T_A(\omega)$ and $T'_B(\omega)$ respectively, where prime and unprimed denote transmission and reception respectively) the received signal $R(\omega)$ can be represented as

$$R = T'_B G T_A S, \tag{2.7}$$

where the frequency dependence (ω) of each function is implied. Deconvolving R with a delta function in time, or applying the inverse filter in the frequency domain, and then propagating again from A to B we get a focal signal

$$F = \frac{T'_B G T_A}{T'_B G T_A S} = \frac{1}{S}, \tag{2.8}$$

The spectral division by $T'_B G T_A S$ is unstable when this function has notches. This instability can be avoided, for example, by a water level regularization [24] where one does the following,

$$\frac{1}{T'_B G T_A S} \rightarrow \frac{(T'_B G T_A S)^*}{|T'_B G T_A S|^2 + \epsilon}. \tag{2.9}$$

Application of the inverse filter can thus also be used for source reconstruction for arbitrary sources (i.e., $S(t) \neq \delta(t)$, or $S(\omega) \neq 1$). To obtain the original source function it is only necessary to invert the focal signal $F(\omega)$ for the frequency domain representation, and inverse Fourier transform to obtain a source reconstruction as a function of time.

In the context of time reversal, the inverse filter is usually used for enhancing the temporal compression, assuming that the source signal was a delta function. By following the derivation above, another application would be to achieve an approximated delta function, limited by available bandwidth, from any source function. To do so requires that the source function be known and multiplied, in the frequency domain, by the result of the inverse filter before broadcasting the signal for focusing. Using the regularization Eqs. 2.9, the focal signal is then equal to

$$F = \frac{S(T'_B G T_A S)^*}{|T'_B G T_A S|^2 + \epsilon} T'_B G T_A \approx 1. \tag{2.10}$$

In the absence of regularization ($\epsilon = 0$), the right hand side would be equal to 1, which corresponds to a delta function $\delta(t)$ in the time domain. A nonzero regularization ($\epsilon > 0$) yields a temporal focus that differs from a true delta function. For bandlimited data, one can, at best, hope to retrieve a bandlimited delta function. By extension, to focus another arbitrary function X from information acquired from the propagation of some other given source S, one can simply perform another multiplication such that the focal signal would be broadcasting the signal for focusing. Thus, using the regularization Eqs. 2.9, the focal signal becomes

$$F = \frac{XS(T'_B G T_A S)^*}{|T'_B G T_A S|^2 + \epsilon} T'_B G T_A \approx X. \tag{2.11}$$

Of course the arbitrary signal X desired for focusing must have a spectral content that lies within the bandwidth of the original controlled, or known, source. Violating this requirement would reduce the fidelity of the reconstruction of X in much the same way that the approximate delta function reconstruction is limited by the bandwidth available from the original source signal.

A final important point to be made here, before proceeding to the experimental validation, is the effect of transducer responses in the TR and IF procedures. From Eqs. 2.8 and 2.10 it is apparent that the transducer responses do not completely cancel in the TR process, and thus there will be some added color to the resulting focal signal. The added color can be

described as a ringing, or multiple converging wave fronts as recently shown by Anderson *et al.* [25] However, this added coloring will be significantly reduced for the IF results as we will show in our experiments. Note that the transducer responses only cancel for reciprocal TR (forward from A to B and then backward from A to B), whereas they don't necessarily cancel for standard TR (forward from A to B and then backward from B to A). Starting with Eq. 2.7 and following through the reciprocal TR process we can see that the focal signal becomes

$$F = (T'_B G T_A S)^* \; T'_B G T_A = |T'_B|^2 |G|^2 |T_A|^2 S^* \tag{2.12}$$

with the * denoting the complex conjugate. Thus in order to get the source reconstruction, one must know the transducer responses at both locations A and B, or use transducers possessing flat frequency responses over the bandwidth of interest, as they each color the focal signal by the square of their frequency responses.

2.3 Experimental Validation: Temporal Characteristics

The purpose of this study is to optimize focusing in experimental situations where only a single channel is used with reverberant signals in a closed cavity. With this in mind, it is prudent to test the methodology experimentally, as presented above. To do this, we used a sample made of fused quartz, $10 \times 10 \times 10$ cm^3. A source transducer (1.27 cm diameter, 2 mm thick piezoelectric disk) was attached to the sample using epoxy. This defines, and fixes, our source position A. The receiver, a non-contact laser vibrometer (PSV 301, OFV 5000 controller, Polytec Inc.), was positioned at a point B on the surface. As we cannot perform a standard TR experiment with a laser vibrometer, since it cannot act as both receiver and source, we performed reciprocal TR experiments, i.e., where the original source and back propagation signals are emitted from the same location/transducer, thus focusing the wave energy to the original, user-selected receiver location. This use of TR in a reciprocal sense is now a widely used form of TR, and indeed is the method originally used by Parvelescu[1] in the first known demonstration of TR in acoustics. It is also the method described analytically

in detail in Sec. 3.2.

The source function, a 5μs shaped toneburst of 200kHz, was broadcast from the source transducer using a 12-bit arbitrary waveform generator with a conversion rate of 10MHz. The response to this impulse was recorded by the laser vibrometer (5mm/s/V, 250kHz bandwidth) using a 14-bit digitizer also sampling at 10 MHz. The generator and digitizer were synced such that the source impulse was centered in a 3.2768 ms window, thus the first portion of the received signal $R(t)$ contains no causal signal. This also means that the TR focus will occur at 1.6384 ms during the rebroadcast. All excitations, i.e., for source, TR and IF broadcasts, are performed at a maximum 100 Vpp.

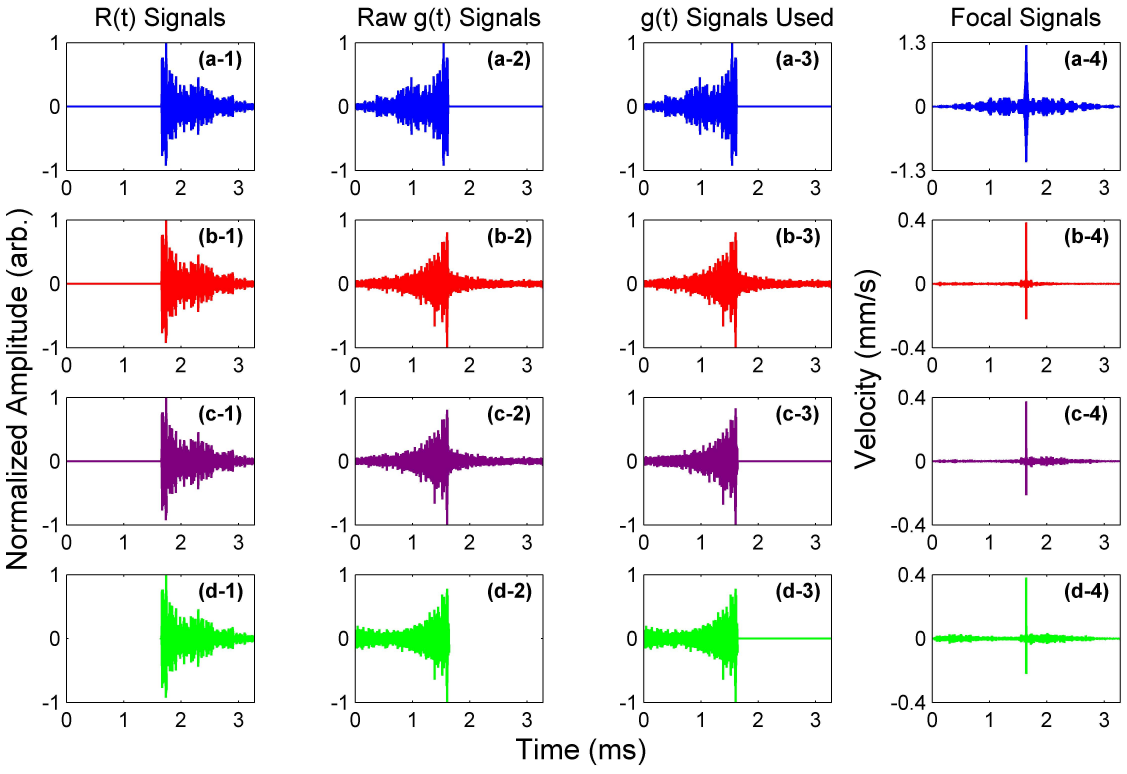

Figure 2.1: Time reversed signals used for back propagation, (a) (blue): original response $R(-t)$ due to a 5μs 200kHz tone burst; (b) (red): full signal $g(t)$ from the deconvolution procedure described herein; (c) $g(t)$ as obtained from utilizing only the causal portion of $R(t)$ and zero padding for the acausal portion; (d) $g(t)$ from (b) with the acausal portion (i.e., $t > 1.6384$ ms) set equal to 0.

Before we directly compare the temporal compression and focus abilities of both TR and the IF, we must first decide what $R(t)$ and $g(t)$ signals to use to create the focusing. In Figure 2.1 we illustrate four different methods of creating a focus of energy. During the forward propagation we record the incident vibration with the laser vibrometer at a location on the surface of the block, which arrives in the latter half of the 3.2768 ms window (see Figure 2.1(a-1)). In reciprocal TR, we simply reverse this signal and broadcast it (see Figure 2.1(a-2) and (a-3)) into the sample with the piezoelectric transducer to achieve focusing at the laser vibrometer location (see Figure 2.1(a-4)). Before broadcasting the signal in reciprocal TR (and in other deconvolution methods) we can amplify the signal to maximize the focusing amplitude. In what we term the full deconvolution process, the deconvolution operation is performed on the full signal recorded during the forward propagation (see Figure 2.1(b-1)) to obtain the signal (see Figure 2.1(b-2) and (b-3)) used to create the focusing (see Figure 2.1(b-4)). Another way to perform the deconvolution method is to take the full deconvolution result (see Figure 2.1(b-2) and (c-2)) and set the second half of the signal ($t > 1.6384$ ms) equal to zero (see Figure 2.1(c-3)) and observe the focusing (see Figure 2.1(c-4)). Finally, if we shorten the acquisition window to only the second half (1.6384 ms $< t \leq 3.2768$ ms), thus avoid any acausal portion of the signal, and use this signal (see Figure 2.1(d-1)) in the deconvolution operation (see Figure 2.1(d-2)), we can then zero pad this signal (see Figure 2.1(d-3), the zero padding is done to ensure that the focal signals in each of the 4 processes are of the same length) before sending it back into the block to observe the focusing (see Figure 2.1(d-4)).

In summary, Figure 2.1 row (a) illustrates the signals used in the reciprocal TR process (blue colored signals), row (b) illustrates the signals used in the full deconvolution process (red colored signals), row (c) illustrates the signals used in the zeroed-acausal-portion deconvolution process (purple colored signals), and row (d) illustrates the signals used in the no-acausal-portion signal deconvolution process (green colored signals). Figure 2.1 column 1 depicts the signals obtained during the forward propagation step ($R(t)$), column 2 depicts

the signals obtained from the deconvolution process ($g(t)$) performed on the signals in column 1, column 3 depicts the signals that we send back into the block after allowing for some processing of the signals in column 2 (such as zeroing out portions of the signal or zero padding them), and column 4 depicts the focal signals from each process ($F(t)$). Note the reduction in amplitude, by a factor of about 3, that results from the deconvolution processes in comparison to the reciprocal TR process.

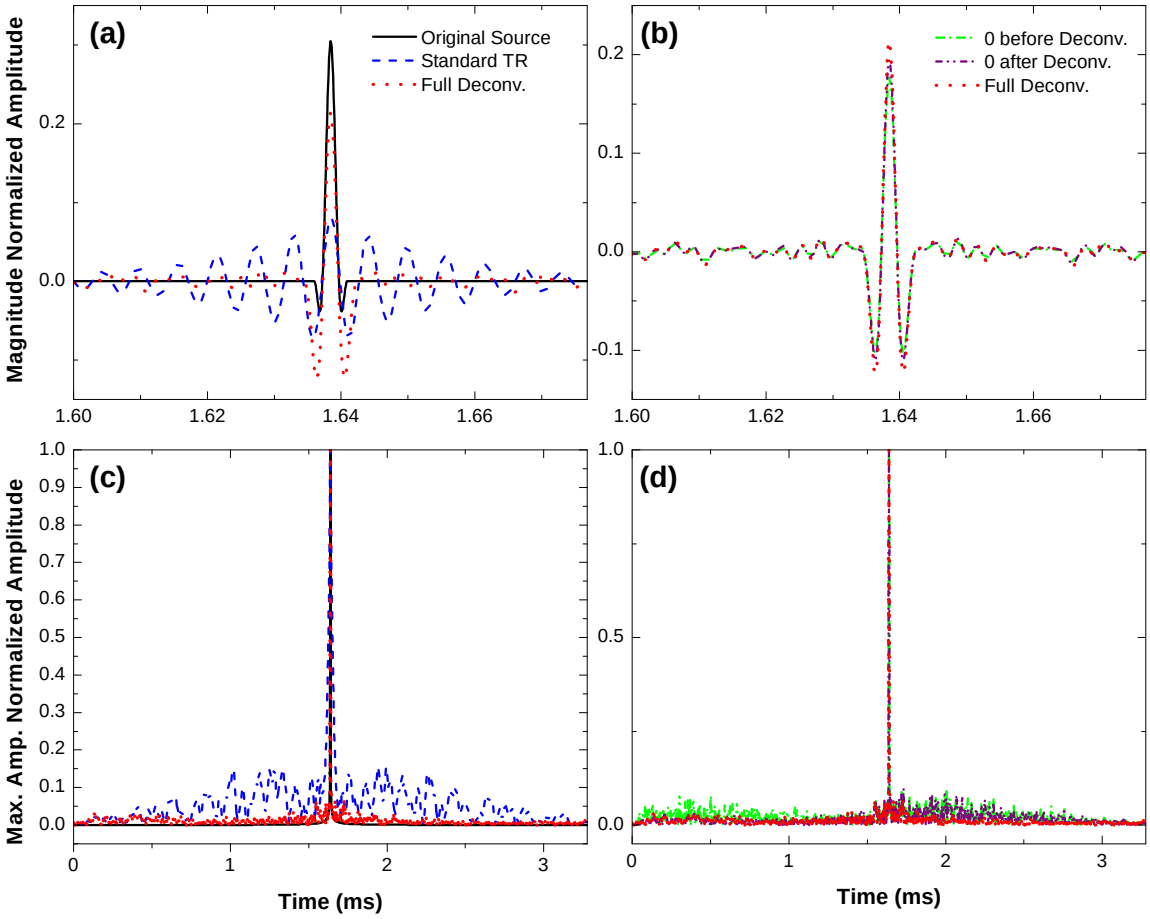

Figure 2.2: Normalized focal signals resulting from the back propagation of the TR signals shown in Figure 2.1, compared with the original source function. (a) & (b) illustrate the structure of the signals near the focal time, each of which have been normalized to the total signal magnitude to accurately compare the temporal compression of the signal. (c) & (d) are envelopes of the focused signals for the entire duration of the signal. Envelopes are presented normalized to the maximum peak amplitude of the velocity to illustrate the difference in perceived signal to noise (i.e., the signal amplitude at the focal time compared to all other times in the signal.)

The focal signals recorded at B due to the broadcast of each of the signals shown in Figure 2.1, column (c), are now compared in Figure 2.2. For clarity the colors used in Figure 2.1 and Figure 2.2 are consistent. The first noteworthy difference lies in the comparison of the original source signal with the focused signals resulting from reciprocal TR and the full deconvolution, Figure 2.2(a). Here we see what has been reported in prior IF studies, i.e., that the IF produces a more temporally compressed focal signal. This is most easily seen by normalizing each signal to the total signal magnitude and calculating the fraction of the amount of energy in the original source ($1.6359 < \tau < 1.6409$ ms). Doing so we find that the original source contained 100% of its energy in that window (by definition), while the TR and IF reconstructions contain 14% and 78% respectively. This can also be seen in the envelopes shown in Figure 2.2(c) over the full signal duration. While this type of quantification is new, this observation has been made previously[26].

In comparing the various deconvolution results, i.e., full, zeroed-acausal-portion, and no-acausal-portion deconvolution processes, we see, Figure 2.2(b), that in the focal interval shown, each method produces an identical result. However, in looking at the entire signal duration, we can see that not employing the acausal signal (either by zeroing it out before back propagation, Figure 2.1 row (c), or by not including the signal recorded before the source emission, Figure 2.1 row (d)) there are undesirable artifacts introduced at times away from the focus (raising the noise floor) decreasing the reconstruction percentage from 78% down to 54% and 63% respectively, indicating that the acausal portions of the signal are highly desirable to be used for any application where high signal fidelity is important or where multiple impulses may be focused successively with little separation, e.g., communications or lithotripsy. The process illustrated in Figure 2.1 row (b) is akin to zero padding the signal used in the deconvolution operation, whereas the processes in rows (c) and (d) do not take advantage of zero padding. Another method used to quantify the improved temporal focus is through signal to noise ratio. We quantify the apparent signal to noise ratio by the ratio of the main maximum and the second largest maximum in the signal. This ratio measures

how well the main maximum stands out above the rest of the signal. For full deconvolution, the ratio is 14.8 (Figure 2.1 (b)-4) and this ratio drops down to 10.2 and 10.3 for the no zero padding result (Figure 2.1 (d)-4) and for the zero padding after deconvolution result (Figure 2.1 (c)-4) respectively. Hence the best processes to use is the full deconvolution that benefits from zero padding.

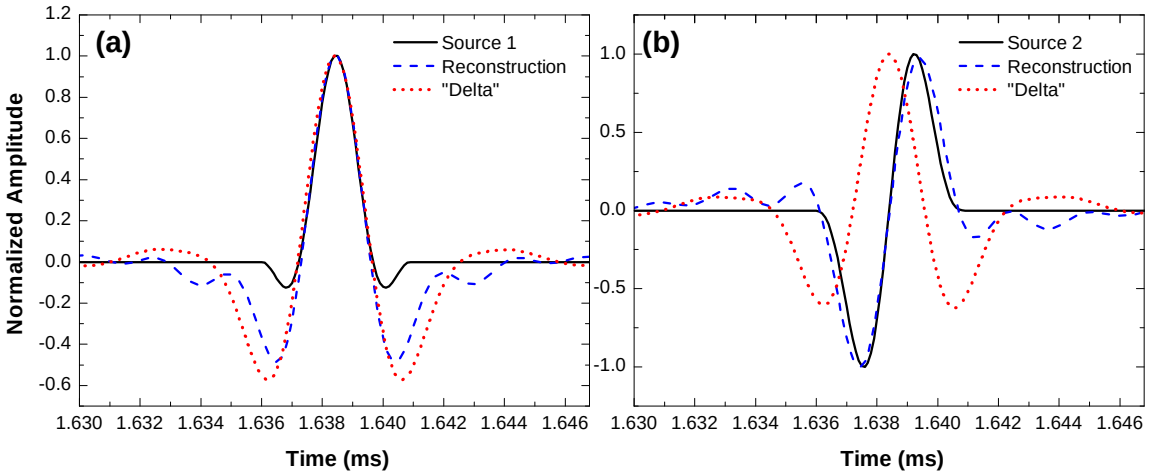

Figure 2.3: Source reconstruction and "delta" function results using deconvolutions. The original source is shown in comparison to the source reconstruction (i.e., from Eq. 2.11) and the delta function approximation (i.e., from Eq. 2.10). (a) Comparison using S_1 a $5\mu s$ 200 kHz toneburst with a maximum at 1.6384 ms. (b) Comparison using a source function S_2 of identical bandwidth to S_1 but with a 90° phase shift.

Before leaving the temporal domain and investigating the effect of the IF on the spatial focusing, we will look at source reconstruction as discussed in Sec. 2.2, Eqs. 2.11 and 2.10. To do so we alter our original source function, which we now call S_1 and is shown in Figure 2.3(a), by applying a phase shift of 90°. We refer to this phase shifted source as S_2 shown in Figure 2.3(b). As the only difference between the two sources is a phase shift, the two sources have equally defined bandwidths, thus the IF filter will apply equally well, or poorly, to the received signals from both. Relevant to our previous results on the implementation of the IF, the reconstruction procedures will employ the full deconvolution, as that has been demonstrated, above, to be the cleanest implementation. Figure 2.3 displays the results of the focusing procedures, i.e., source reconstruction and limited band delta function, compared

to the two original source functions. A comparison of Figure 2.3(a) and (b) shows that employing Eq. 2.11 produces a very good approximation of the original source functions. When multiplying by the source function prior to back-propagation, we can verify that the original phase information of the source is lost and the focal signal approximates a delta function to the extent possible with the available bandwidth. The fact that a true single point delta function is not achieved is of no surprise, as finite signal length and available bandwidth make this effectively impossible by any means.

In conclusion, the initial main objective for the use of deconvolution has been to improve the temporal focusing. We showed experimentally that simple deconvolution can achieve this. Beyond improving temporal compression of the focal signal, we also showed that the details of implementation of the IF is important, with the most robust being what we refer to as a full deconvolution. Finally, we showed the ability of the IF to be used for arbitrary source reconstruction or delta function approximation. All of the above demonstrations were limited to time domain observations. In the next section, we present one explanation, and supporting observations, for the improvement of spatial focusing with improved temporal compression.

2.4 Improved temporal focusing leads to improved spatial focusing

In this section, we show that better temporal focusing implies better spatial focusing for the spherical average of the focus. We begin by first considering the wave field near its focal spot at $r = 0$ and consider the medium to be locally homogeneous in that region. The solution of the Helmholtz equation in an acoustic, homogeneous medium can be written as

$$p(r, \theta, \varphi, \omega) = \sum_{l=0}^{\infty} \sum_{m=-l}^{m=l} a_{lm} j_l(kr) Y_{lm}(\theta, \varphi) \ , \tag{2.13}$$

see Table 8.2 of Ref. [27]. In this expression j_l denotes the spherical Bessel function, Y_{lm} the spherical harmonics, and $k = \omega/c$, where c is the wave speed. According to expressions (11.144) and (11.148) of Ref. [27], $j_l(0) = 0$ for $l \geq 1$ and $j_0(0) = 1$. This allows us to investigate the focus of the wavefield by looking at the spherically symmetric component

$l = 0$. Using $Y_{00} = 1/\sqrt{4\pi}$ (Table 12.3 of Ref. [27]), this means that at the focal point

$$p(r = 0, \theta, \varphi, \omega) = \frac{a_{00}}{\sqrt{4\pi}} \, . \tag{2.14}$$

The properties of the wave field at the focal point thus only depend on the coefficient a_{00}. Since the $l = m = 0$ component of the spherical harmonics expansion gives the spherically symmetric component of the wave field, the properties of the wave field at the focal point can only bear a relation to the spherically symmetric component of the wave field ($l = m = 0$). The properties of temporal focusing can thus only be related to the spherically symmetric component of the spatial focusing.

In the following, we only analyze the spherically symmetric component $p_{l=0}(r, t)$ of the focus, because according to Figure 2.4 (a) and (b), the central focal spot is nearly spherically symmetric. Using that $j_0(kr) = \sin(kr)/kr$, the spherically symmetric component of Eq. (2.13) is given by

$$p_{l=0}(r, \omega) = p_0 \, \frac{e^{-ikr} - e^{ikr}}{r} \, , \tag{2.15}$$

with $p_0 = -a_{00}/(2ik\sqrt{4\pi})$. The coefficient p_0 depends on frequency. Using the Fourier convention $f(t) = \int p_0(\omega) e^{-i\omega t} d\omega$, and using that $k = \omega/c$, Eq. (2.15) corresponds, in the time domain, to

$$p_{l=0}(r, t) = \frac{f(t + r/c) - f(t - r/c)}{r} \, . \tag{2.16}$$

In this equation, $f(t + r/c)$ denotes the wave that is incident on the focus, and $f(t - r/c)$ the outgoing wave once it has passed through the focus. The field at the focus follows by Taylor expanding $f(t \pm r/c)$ in r/c and taking the limit $r \to 0$, this gives

$$p_{l=0}(r = 0, t) \approx \frac{2}{c} f'(t) \, . \tag{2.17}$$

In this expression and the following, the prime denotes the time derivative. Equation (2.17) states that the wave field at the focus is the time derivative of the incoming wave field.

Equation (2.17) gives the temporal properties of the focus. In order to get the spatial properties, we consider the wave field near the focal point at time $t = 0$. Setting $t = 0$ in

Eq. (2.16), and making a third order Taylor expansion of $f(\pm r/c)$ gives

$$p_{l=0}(r, t=0) \approx \frac{2}{c} f'(0) + \frac{r^2}{3c^3} f'''(0) \ . \tag{2.18}$$

where the prime denotes a time derivate. Using Eq. (2.17) to eliminate f, gives

$$p_{l=0}(r, t=0) \approx p_{l=0}(r=0, t=0) + \frac{1}{6c^2} p''_{l=0}(r=0, t=0) r^2 \ . \tag{2.19}$$

This is a parabolic approximation for the wave field near the focus, with coefficients related to the wave field and the focus and its second time derivative. The radius R of the focal spot can be estimated by setting the left hand side of Eq. (2.19) equal to zero, this gives

$$R \approx \sqrt{6c^2} \sqrt{\frac{-p_{l=0}(r=0, t=0)}{p''_{l=0}(r=0, t=0)}} \ . \tag{2.20}$$

A good temporal focusing means that the temporal curvature of the wave field at the focal point is strong, this means that $-p''/p$ is large, and that the radius R is small. Good temporal focusing thus implies that the radius in the spherically symmetric part of the spatial focus is small.

This claim of improved spatial focusing accompanying improved temporal compression can be experimentally observed by measuring the wave fields produced in the two focusing procedures, TR vs. IF. The surface of the fused quartz block was scanned with a laser vibrometer while each type of focus was produced. The improvement in the temporal focal quality of the IF procedure over TR has already been shown in Figure 2.1 and Figure 2.2. Figure 2.4 displays the comparisons of the spatial extent of the two focusing procedures obtained with the scanning laser. The cross sectional displays of the data in Figure 2.4(c) and (d) show that the IF focus is 20-30% narrower as measured at half of the respective maxima (i.e., 2-3 mm over 1 cm).

While the spatial extent of the focus appears to be smaller using the IF method, confirming the theory of improved temporal compression resulting in improved spatial focusing, two other features are also noticeable. First, in no particular order, is the larger degree of uniformity (≈ 0) of the IF wave field away from the focus, while the TR focus is much

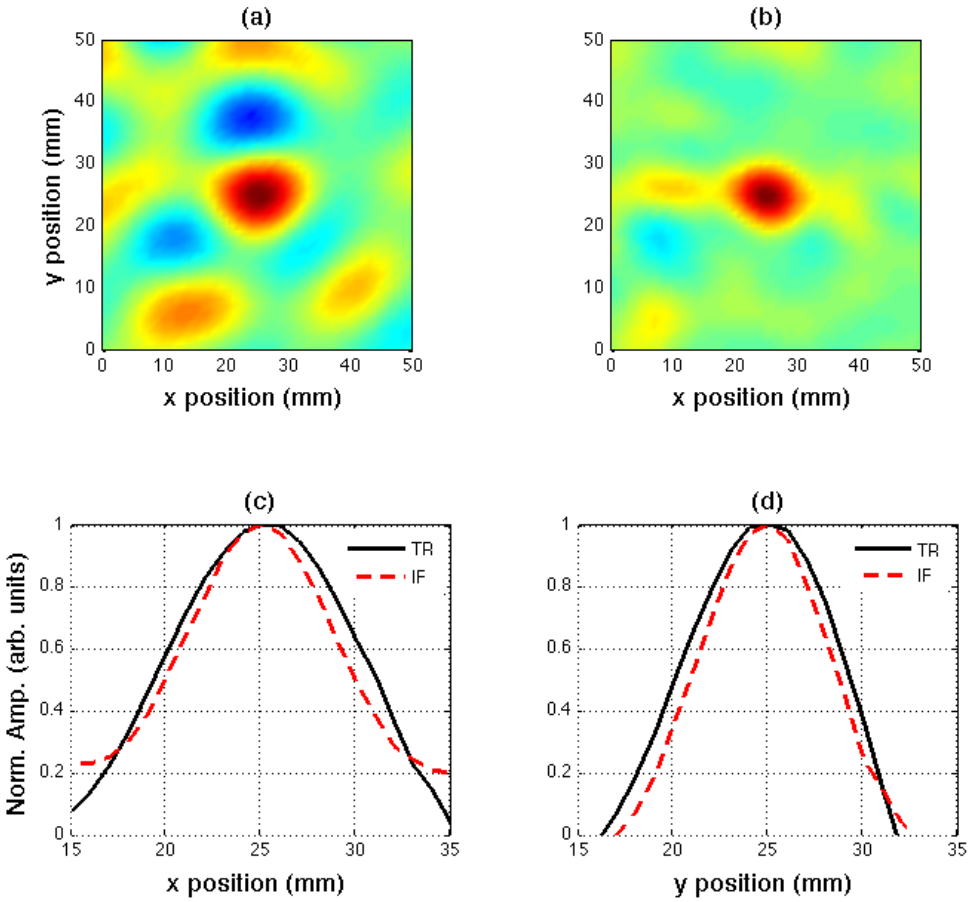

Figure 2.4: (a) two dimensional image of the wave field at the time of focus using classical TR. (b) two dimensional image of the wave field at the time of focus using the IF. (c) one dimensional line-outs from (a) and (b) at $y = 25$ mm. (d) one dimensional line-outs from (a) and (b) at $x = 25$ mm.

more structured across the imaged region. Second is the fact that the maximum achieved amplitude using the IF is only half that of the TR method, despite the fact each signal was normalized and rescaled to the same maximum voltage (100 Vpp) prior to rebroadcast.

2.5 Conclusion

Here we have introduced a simple method for determining the optimal signal to be used in a TR experiment in order to maximally compress the focus as an approximate delta function (with limited bandwidth) in both time and space or for optimal signal reconstruction. Creation of an approximate delta function technically requires knowledge of the source signal, whereas source reconstruction requires a second inverse filter operation in post processing. Previous implementations of the inverse filter operation avoided the need to know the source signal by utilizing impulse like source signals. This method has been experimentally verified, albeit without fully varying all possible parameters. A more detailed study is currently underway to quantify the effects due to variations in available bandwidth, and material properties (e.g., homogeneous vs. heterogeneous media, range of attenuations, wave speeds, length of scattered signal used, etc.)

While temporal and spatial focusing have been enhanced with this method, there is a cost in the maximum achieved amplitude, $A_{TR} \approx 2A_{IF}$. This fact, coupled with the effect of the *acausal* portion of $g(t)$ may lead one to think simplistically about $g(t)$ as containing a signal to focus the energy at the appropriate time and place, and another signal that, simultaneously, actively cancels *noise* at all other times and locations. Thus the IF focus is cleaner and more impulse-like, but not as strong, as some of the energy being transmitted is exerted in suppressing sidelobes, spatially and temporally.

We have also shown, theoretically and experimentally, that if one has good temporal focusing, the radius in the spherically symmetric part of the spatial focus is small. This concept can turn out to be useful in future research because it allows one to work on improving the temporal focusing in order to improve the spatial focusing, e.g., communicating to a precise location or focusing high intensity ultrasound for lithotripsy without damaging

the surrounding area, to name a few. When the focal spot is far from being spherically symmetric, as may be the case where the receiver aperture is small, an improved temporal focus does not necessarily imply an improved spatial focus.

CHAPTER 3
IMPROVED TEMPORAL FOCUSING AT SOURCE LOCATION USING DECONVOLUTION

Time reversal techniques are used in ocean acoustics, medical imaging and non-destructive evaluation to backpropagate recorded signals to the source of origin. We demonstrate experimentally a technique which improves the temporal focus achieved at the source location. The experiment consists of propagating a signal from a transducer within a concrete block to a single receiver on the surface, and then applying time reversal or deconvolution to focus the energy back at the source location. The results show that we are able to generate a focus in time at the correct location. The proposed method is simple and proven to be robust. Additionally, its costs are negligible due to deconvolution being a preprocessing step to the recorded data. The technique can be applied for detailed investigation of the source mechanisms (e. g. cracks) but also for monitoring purposes.

3.1 Introduction

Several methods are used to evaluate acoustic signal generated by events in media such as water, rocks, metals or concrete. Most of them are summarized as acoustic emission methods (AE), mainly travel time evaluation methods to localize the point of origin. Sophisticated methods have been developed in seismology to localize and characterize earthquakes. Time Reversal (TR) has been the focus of much research in acoustics due to its ability to compress the measured scattered waveforms back at the source point in both space and time [1–4].This has led to TR being applied in a wide variety of fields such as medicine, communication or nondestructive evaluation. However, continued work is being done to improve TR ability to focus energy. Some newly developed techniques use an array of input transducers, measure the wave field with an array near the desired focal spot, and then optimize the spatial and temporal focusing [[8–11, 14–16]. Other methods use an array of input transducers and

optimize the temporal focusing at an output transducer [17–21]. However, these techniques can require/benefit from large arrays while simultaneously loosing spatial localization in order to enhance temporal focusing.

In this paper, we design and execute an evaluation experiment to compare conventional time reversal to an improved variant which uses deconvolution (DC). We explore the application of DC, which is a primitive though robust version of the inverse filter [8, 12], to calculate the optimal signal for backpropagation. The experiment consists of a concrete block which has a sources embedded within. Instead of using a large array of receivers, the experiment uses only a single receiver to record the scattered waveform. TR or DC is then applied to the measured scattered waveform to calculate the TR and DC signal. The calculated signals are then backpropagated from a transducer on the surface of the block into the medium and recorded at the original source location transducer. By this experiment, we are able to explore and compare the capabilities of TR and DC to focus the measured waveforms at a point in both space and time. We show that DC significantly improves the temporal focus compared with TR.

3.2 Theory: Deconvolution

Time reversal (TR) is a process used to compress the measured scattered waveforms at a point in both space and time to ideally a dirac delta function $\delta(t)$. It uses the recorded impulse response which can be represented by a Green function G_{AB} between two points A and B. TR then simply reverses the signal in time and propagates it back from the receiver location into the same medium. By doing so, one expects the energy to focus at the source location. The TR process can be represented by the following equation,

$$\int_{-\infty}^{\infty} G_{AB}(\tau) G_{AB}(\tau - t) d\tau = \delta(t) \ , \tag{3.1}$$

where reciprocity has been used to replace the Green function G_{BA} with G_{AB}. According to equation 3.1, the TR process, which is the autocorrelation of $G_{AB}(t)$, should equal a delta function. However, in practice, one cannot truly recreate a dirac delta function focus due to

one or more conditions, necessary to satisfy Eq. 3.1, not upholding. In order for it to work perfectly, one must record for infinite time, Green's functions are assumed to contain flat, infinite bandwidth, and one must have full coverage of the wavefield. These requirements are not upheld during an experiment. This led us to explore the application of deconvolution.

Going back to Eq. 3.1, we can rewrite this (using a convolution notation, rather than the integral form) as

$$F(t) = g(t) \star R(t) \approx \delta(t) \ , \tag{3.2}$$

where $F(t)$ is the focal signal or source reconstruction, $R(t)$ is the recorded signal measured at the receiver location B from the initial source propagation, and $g(t)$ is the signal necessary to be back propagated for focusing. We are able to go from Eq. 3.1 to Eq. 3.2 because we only investigate signals between the two points A and B, and remove the green function notation to indicate we do not have infinite bandwidth. Thus, we remove some of the unrealistic conditions that Eq. 3.1 required. For a TR process, the signal for backpropagation is purely the time reversed recorded signal $g(t) = R(-t)$. Our goal is to calculate the optimal signal $g(t)$ such that the focal signal $F(t)$ approximately equals a dirac delta function $\delta(t)$.

Deconvolution equates to inverse filtering by transforming to the frequency domain, thus Eq. (3.2) becomes

$$F(\omega) = g(\omega)R(\omega) \approx 1 \ . \tag{3.3}$$

Equation 4.3 is used to solve for $g(\omega)$,

$$g(\omega) = \frac{1}{R(\omega)} = \frac{R^*(\omega)}{|R(\omega)|^2}, \tag{3.4}$$

where $*$ denotes a complex conjugate operation. This expression gives a mathematical expression for $g(\omega)$. However, this result is unrealistic for experimental use in the event that there is a limited bandwidth, significant background noise, or more specifically, if $R(\omega) = 0$ at any frequency. To avoid this singularity issue, we add a constant to the denominator to

ensure that we never divide by 0, hence Eq. 3.4 becomes,

$$g(\omega) = \frac{R^*(\omega)}{|R(\omega)|^2 + \epsilon}\ , \tag{3.5}$$

where ϵ is a constant related to the original received signal as

$$\epsilon = \gamma\ \text{mean}(|R(\omega)|^2). \tag{3.6}$$

The quantity γ, which is sometimes referred to as the waterlevel parameter [24], is an arbitrary constant chosen to optimally reduce the effect of noise introduced through the DC procedure. Here we use $\gamma = 0.9$ for all experiments. The value 0.9 was chosen based on optimizing the focus energy in a process similar to that developed by Clayton *et al.*[24]. Eq. 3.6 provides one with the solution for $g(w)$. One only has to inverse fourier transform this result to retrieve the "optimal" DC signal in the time domain to be backpropagated such that one gets a approximate dirac delta function focus.

3.3 Experimental Set up

The purpose of our study is to explore the application of the deconvolution variant compared to conventional time reversal in focusing energy at a source location within a sample. In order to make such comparison, we created the following experimental set up. A 30 by 30 by 37 cm concrete block had been casted from 72 kg Quickcrete mix (No. 1101, max aggregate grain size $<$ 4 mm), about 60 l water and 5 kg additional gravel (5-15 mm grain size). Three ultrasonic piezo transducers (proprietary type Acsys S0807, center frequency 60 kHz, ES in Figure 3.1) were positioned inside the formwork in various orientations before concreting. The block contains only minimal reinforcement, mainly to hold the embedded sensors in place while pouring the concrete. Broadband Acsys point contact sensors type S1803 (center frequency about 100 kHz, PT in Figure 3.1) were used as external transducers. They are piezo based as well and feature a spring loaded 2 mm diameter ceramic tip for contact to the concrete. They are sensible to acceleration vertical to the concrete surface. The transmitter signal is generated by custom made rectangular signal generator/amplifier

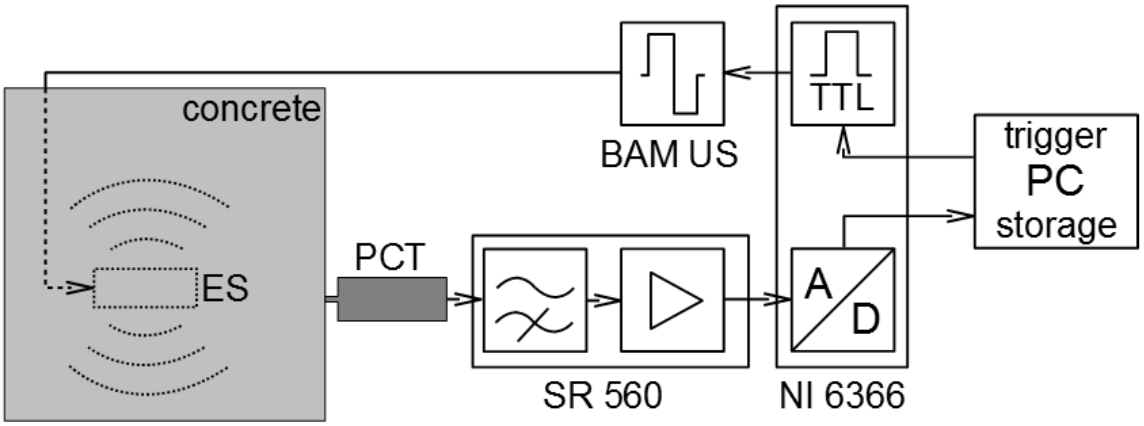

(a) Acquisition workflow

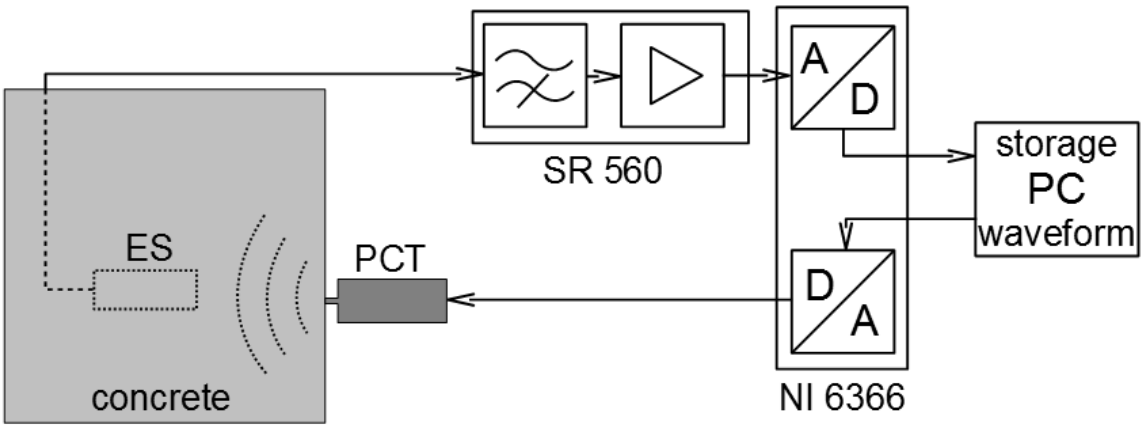

(b) Backpropagation workflow

Figure 3.1: Diagram indicating tools and methods used during acquisition and backpropagation.

(BAM US in Figure 3.1) triggered by a TTL impulse issued by our data acquisition device (National Instruments model 6366). Signals received by the external sensors are 1 kHz low pass filtered and amplified by a Stanford Research low noise preamplifier (SR 566) before being digitized and recorded. The workflow and set up used for acquiring the data is shown in Figure 3.1(a). For backpropagation, the setup is reversed. The BAM US device is removed. The transmitter signal generated is replaced by the digital/analog converter integrated in the data acquisition device, sending the computed, time reversed/deconvolved waveforms to the external sensor. The embedded sensor is used as receiver, again using the preamplifier before AD conversion and recording. This reversed set up is shown in Figure 3.1 (b).

We have used a sampling frequency of 2 MHz and 20000 samples per trace (10 ms recording time). A 4000 sample (2 ms) pretrigger interval was set. Amplitude resolution is 16 bit. True zero time of the transmitter could be identified by electromagnetic crosstalk between transmitter and receiver cables, generating a small but easy to recognize impulse in the receiver data.

Note, that due to a high noise lab environment and a lack of a power amplifier for the backpropagated transmitter signal we had to apply an additional 2 kHz low-pass Butterworth filter on all data.

3.4 Discussion

Our experiments started with propagating a defined 60 kHz source function from the embedded source towards the external receiver. Note the pretrigger time present in recorded signal shown in Figure 3.2. This pretrigger time was proven by Ulrich *et al* [28] to be necessary if one desires to use DC for any application where high signal fidelity is important or where multiple impulses may be focused successively with little separation. Additionally, it was shown by Ulrich *et al* [28] that the acausal portion of the signal is necessary in order to create a symmetric focus.

Once our wave field was recorded at the single receiver, TR or DC was applied to calculate the back propagating signals. Applying these two methods, one achieves the results

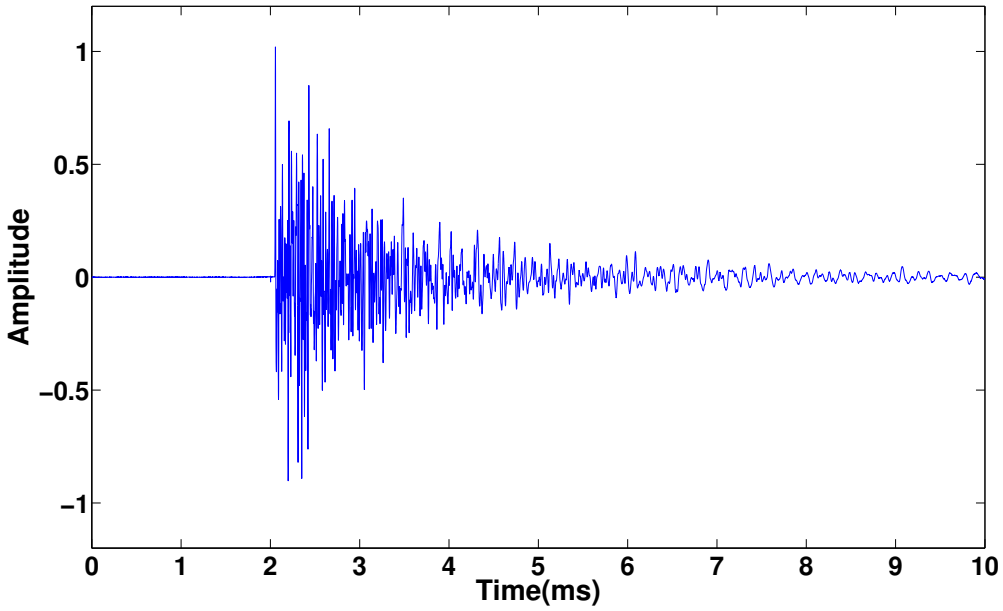

Figure 3.2: Recorded scattered waveform at a single receiver on the surface of a concrete block due to our source function generation from the embedded source transducer.

shown in Figure 3.3 where (a) highlights the backpropagating signal calculated using TR while (b) shows the DC back propagation signal. These two signals shown in Figure 3.3 differ significantly in one feature: TR has zero values past approximately 8 ms while DC's backpropagation signal is nonzero for this time range. This is due to the acausal nature of the recorded signal.

These signals were then backpropagated from the receiver location into the same medium where the receiver on the surface of the concrete block now acted as a source. Propagating these calculated TR and DC signals back into the medium, one would expect a focus at the source location. Figure 3.4 shows the focuses recorded at the source location by using the embedded transducer as a receiver during the backpropagation. Figure 3.4 (a) shows the temporal focus recorded using the TR calculated signal while Figure 3.4 (b) represents the temporal focus achieved using the DC calculated signal. The temporal focus achieved using TR has significant side lobes present away from the time of focus. However, the temporal focus achieved using DC has suppressed most of these side lobes and was able to produce a

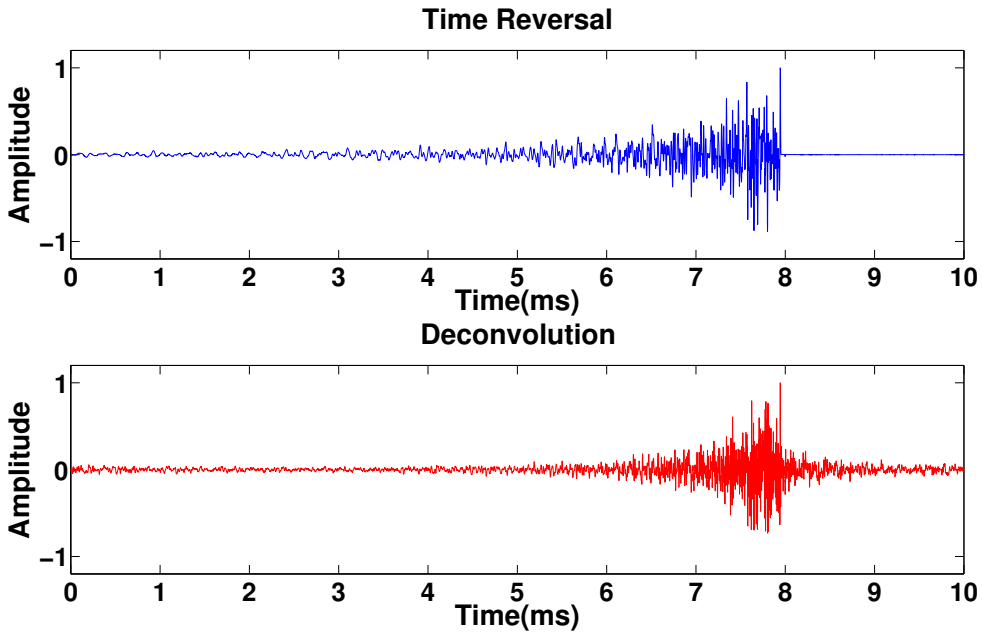

Figure 3.3: Back propagation signals calculated using a)Time Reversal and b) Deconvolution using only the recorded data at the single receiver.

better focus. In order to quantify this improvement, we calculate the amount of energy in a .02ms window around the time of focus compared to the total energy of the signal. The temporal focus achieved using TR only had 41 % of the total energy within this window while DC's temporal focus had 80 % of the total energy within this window. Thus, DC is clearly able to generate a significantly better temporal focus than TR.

In order to proof the robust nature of this method, we reran the experiment using a different location for the receiver (placing the receiver on a different side of the block). The purpose of this experiment was to not only test and make sure DC still had an improved temporal focus compared to TR but to also demonstrate our decision for γ which was the regularization constant. For this set up, DC's temporal focus was 79 % while TR had a temporal focus of 47 %. We would not expect to see the exact same temporal focusing numbers as before because we changed the direction of displacement we record and the distance between the source and receiver. We reran the experiment numerous times, recalculating the DC signal using different values for γ, and recording the temporal focus at the source

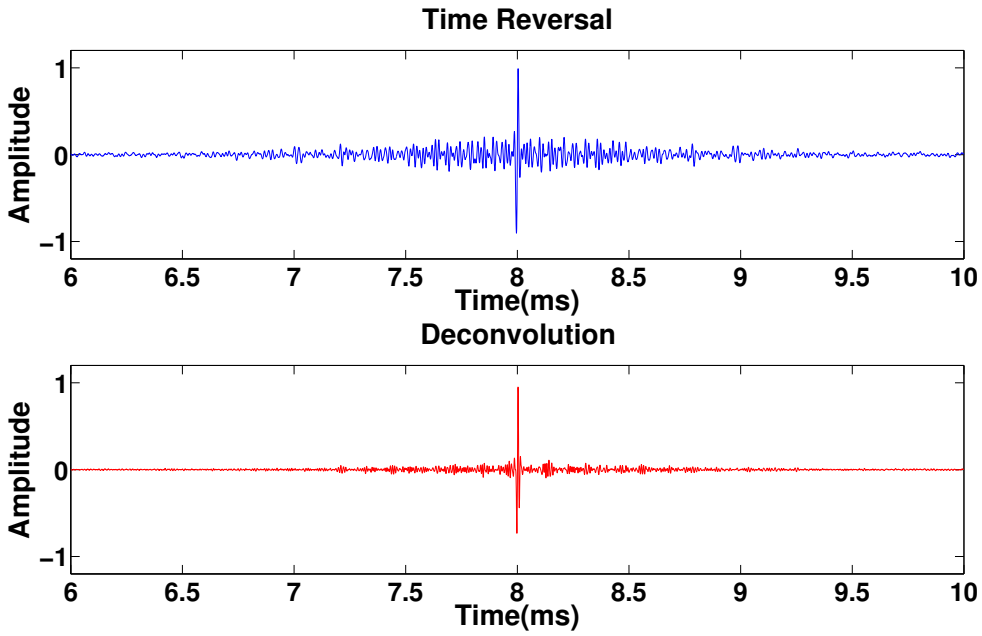

Figure 3.4: Temporal focus measured at the embedded source location using a) Time Reversal, and b) Deconvolution.

location. The experiment showed that the optimal value to be $\gamma = 0.9$. However, even for different γ values, one still achieves some form of a temporal focus until the γ values becomes too small where too much noises gets included into the focus.

The purpose of using time reversal (TR) and deconvolution (DC) processes is to generate a signal such that it will focus at the source location. One can use this feature of the methods for a range of applications in order to characterize the medium. For example, after the time of focus, the wave field will propagate away from the source location with the characteristic as if it were generated by a source mechanism at the focused event location. This is defined as a "virtual" source. This "virtual" source can then be used to for a wide variety of applications from multiple suppression, to medium characterization [29–33]. Additionally, one can continuously monitor and backpropagate signals to investigate the changes occurring within the medium. Finally, using DC, one can define the type of source function focus that will occur at the event location. This was shown to work in Ulrich *et al* [28]Therefore, one could determine the frequency of the focused wave field and allow different frequency

focuses to occur. One then records the scattered wave field generated by the virtual sources consisting of different frequencies to characterize the medium. Therefore, by using DC, we could potentially improve the characterization of the medium compared with TR. In addition, the amplitude can be varied to study nonlinear effects.

3.5 Conclusion

We have introduced a simple though robust method for determining the optimal signal for backpropagation such that one gets an improved temporal focus at the source location. This was proven to hold true for an experimental set up having the source embedded within a concrete block and using only a single receiver. The method does not require any information about the medium. It only needs the recorded signal in order to generate the optimal signal for back propagation. Due to the simplicity, low cost, and robust nature of this method, one could easily implement this technique into pre-existing workflows. This method may then be used to characterize the medium through use of "virtual" sources, repeated backpropagation or backpropagating with different source function focuses.

CHAPTER 4

EVENT LOCATING USING DECONVOLUTION: EXPERIMENTAL APPLICATION AND ANALYSIS

Time reversal techniques are used in ocean acoustics, medical imaging, seismology, and non-destructive evaluation to backpropagate recorded signals to the source of origin. We demonstrate experimentally a technique which improves the temporal focus achieved at the source location by utilizing deconvolution. One experiment consists of propagating a signal from a transducer within a concrete block to a single receiver on the surface, and then applying time reversal or deconvolution to focus the energy back at the source location. Another two experiments are run to study the robust nature of deconvolution by investigating the effect of changing the stabilization constant used in the deconvolution and the impact multiple sources have upon deconvolutions' focusing abilities. The results show that we are able to generate an improved temporal focus at the source transducer using deconvolution while maintaining the robust nature of time reversal. Additionally, deconvolution's costs are negligible due to it being a preprocessing step to the recorded data. The technique can be applied for detailed investigation of the source mechanisms (e.g. cracks) but also for monitoring purposes.

4.1 Introduction

Several methods are used to evaluate acoustic signal generated by events in media such as water, rocks, metals or concrete. Most of them are summarized as acoustic emission methods (AE), which are used to localize and characterize the point of origin of the events. Sophisticated methods have been developed in seismology to localize and characterize earthquakes. Time Reversal (TR) has been a topic of much research in acoustics due to its robust nature and ability to compress the measured scattered waveforms back at the source point in both space and time [1–4]. This has led to TR being applied in a wide variety of fields

such as medicine, communication, ocean acoustics, seismology or nondestructive evaluation. However, continued work is being done to improve TR's ability to focus energy. Some newly developed techniques use an array of input transducers, measure the wave field with an array near the desired focal spot, and then optimize the spatial and temporal focusing [8–11, 14–16]. Other methods use an array of input transducers and optimize the temporal focusing at an output transducer [17–21].

In this paper, we design and execute evaluation experiments to compare conventional time reversal to an improved variant which uses deconvolution (DC). We explore the application of DC, which is a primitive though robust version of the inverse filter [8, 12], to calculate the optimal signal for backpropagation. The ultrasound experiments are performed on a concrete block which has sources embedded within. Instead of using a large array of receivers, the experiments use only a single receiver to record the scattered waveforms. TR or DC is then applied to the measured scattered waveforms to calculate the TR and DC signal. The calculated signals are then backpropagated from a transducer on the surface of the block into the medium and recorded at the original source location transducer. By this experiment, we are able to explore and compare the capabilities of TR and DC to focus the measured waveforms at a point in both space and time. We show that DC significantly improves the temporal focus compared with TR. We also run two different experiments to study the robust nature of deconvolution by investigating the effect of changing the stabilization constant used in the deconvolution and the impact multiple sources has upon deconvolutions' focusing abilities.

4.2 Deconvolution Theory

Time reversal (TR) is a process used to compress the measured scattered waveforms at a point in both space and time to ideally a Dirac delta function $\delta(t)$. It uses the recorded impulse response which can be represented by a Green function G_{AB} that accounts for the wave propagation between two points A and B. TR then simply reverses the signal in time and propagates it back from the receiver location into the same medium. By doing so, one

expects the energy to focus at the source location. The TR process can be represented by the following equation,

$$\int_{-\infty}^{\infty} G_{AB}(\tau) G_{AB}(\tau - t) d\tau = \delta(t) \ , \tag{4.1}$$

where reciprocity has been used to replace the Green's function G_{BA} with G_{AB}. According to equation 4.1, the TR process, which is equivalent to the autocorrelation of $G_{AB}(t)$, should ideally lead to equal a delta function. In practice, however, one cannot truly recreate a Dirac delta function focus due to one or more conditions, necessary to satisfy Eq. 4.1, not upholding. In order for it to work perfectly, one must record for infinite time, Green's functions are assumed to have a flat, infinite bandwidth, the medium is not attenuative, and one must have full coverage of the wavefield at a surface surrounding the points A & B. These requirements are not upheld during an experiment. This led us to explore the application of deconvolution.

We can rewrite Eq. 4.1 in a more generalized form (using a convolution notation, rather than the integral form) as

$$F(t) = g(t) \star R(t) \approx \delta(t) \ , \tag{4.2}$$

where $\star$ denotes convolution, $F(t)$ is the focal signal or source reconstruction, $R(t) = G_{AB}(t) \star S(t)$ is the recorded signal measured at the receiver location B from the initial source propagation, and $g(t)$ is the signal necessary to be back propagated for focusing. We are able to go from Eq. 4.1 to Eq. 4.2 because we only investigate signals between the two points A and B, and remove the Green function notation to indicate we do not have infinite bandwidth. Thus, we remove some of the unrealistic conditions that are required for Eq. 4.1 to hold. For a TR process, the signal for backpropagation is purely the time reversed recorded signal: $g(t) = R(-t)$. Our goal is to calculate the optimal signal $g(t)$ such that the focal signal $F(t)$ approximately equals a Dirac delta function $\delta(t)$.

Deconvolution equates to inverse filtering by transforming to the frequency domain, thus Eq. (4.2) becomes

$$F(\omega) = g(\omega)G(\omega)S(\omega) \approx 1 \ . \tag{4.3}$$

Equation 4.3 is used to solve for $g(\omega)$,

$$g(\omega) = \frac{1}{G(\omega)S(\omega)} = \frac{G(\omega)^* S(\omega)^*}{|G(\omega)S(\omega)|^2}, \tag{4.4}$$

where $*$ denotes complex conjugation. Eq. 4.4 is, however, unrealistic for experimental use in the event that there is a limited bandwidth, significant background noise, or more specifically, if $R(\omega) = 0$ at any frequency. To avoid the associated singularity, we add a constant to the denominator of the last term of eqn. 4.4 to ensure that we never divide by 0, hence Eq. 4.4 becomes,

$$g(\omega) = \frac{G(\omega)^* S(\omega)^*}{|G(\omega)S(\omega)|^2 + \epsilon} \ , \tag{4.5}$$

where ϵ is a constant related to the original received signal as

$$\epsilon = \gamma \ \text{mean}(|G(\omega)S(\omega)|^2). \tag{4.6}$$

The quantity γ, which is sometimes referred to as the waterlevel parameter [24], is a constant chosen to optimally reduce the effect of noise introduced through the DC procedure. Here we use $\gamma = 0.9$ for all experiments. The value 0.9 was chosen based on optimizing the focus energy in a process similar to that developed by Clayton *et al.*[24]. Equation 4.5 gives the solution for $g(\omega)$. One only has to inverse Fourier transform this result to retrieve the "optimal" DC signal in the time domain to be backpropagated such that one gets a approximate Dirac delta function focus.

4.3 Experimental Set Up

A labratory experiment was created, and run in the Civil Engineering lab of Colorado School of Mines. A 30x30x37 cm^3 concrete block was cast from 72 kg Quickcrete mix (No. 1101, max aggregate grain size < 4 mm), with about 60 liters of water and 5 kg of additional

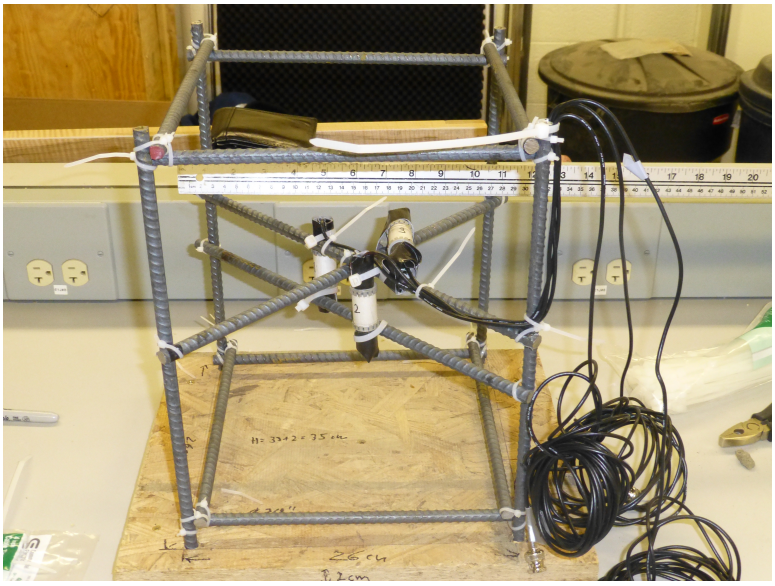

(a) Source set up and reinforcement placed within the concrete block

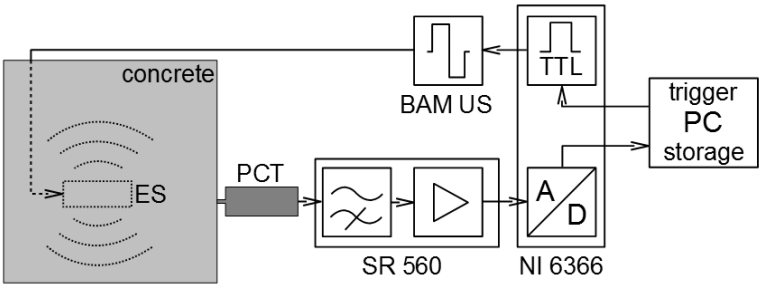

(b) Acquisition workflow

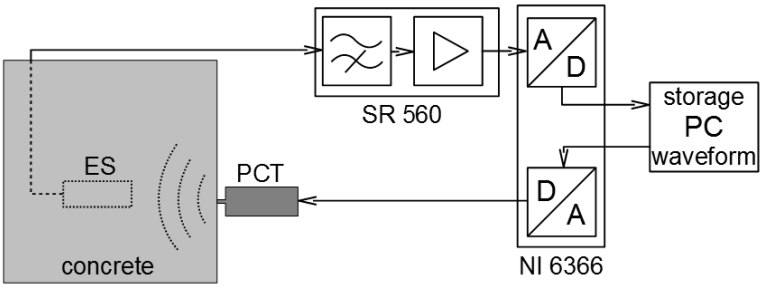

(c) Backpropagation workflow

Figure 4.1: Diagram indicating tools and methods used during acquisition and backpropagation.

gravel (5-15 mm grain size). The block contains only minimal reinforcement as shown in Figure 4.1(a).Three ultrasonic piezo transducers (type Acsys SO807, center frequency 60 kHz, labeled ES in Figure 4.1) were attached to the minimal reinforcement in order to cast them within the concrete block. These sources (transducers) are visible in Figure 4.1(a). These sources were oriented differently in order to generate more complex waveforms and to study the effect of varying source orientation. Source 3 was oriented perpendicular to the other two sources. Broadband Acsys sensors type 1803 (center frequency about 100 kHz, labeled PT in Figure 4.1) were used as external transducers. They are piezo-based and feature a spring-loaded 2 mm diameter ceramic tip for contact to the concrete. These transducers are most sensitive in the direction perpendicular to the surface it is attached to. The transmitted signal is generated by a custom made rectangular signal generator/amplifier (BAM US in Figure 4.1). It is triggered by a TTL impulse which is issued by our data acquisition device (National Instruments model 6366). The recored signals at the external sensor are first low pass filtered at a frequency of 1kHz and amplified by a Stanford Research low noise preamplifier (SR 566) before being digitized and recorded. This was necessary to remove low frequency noise present in our data. The workflow and set up used for acquiring the data is shown in Figure 4.1(b).

For backpropagation, the setup is reversed. The BAM US device is removed. The transmitter signal generator is replaced by the digital/analog converter integrated in the data acquisition device, sending the computed, time reversed/deconvolved waveforms to the external sensor. The embedded sensor is used as receiver, again using the preamplifier before AD conversion and recording. This reversed set up is shown in Figure 4.1 (c). We have used a sampling frequency of 2 MHz and 20,000 samples per trace (10 ms recording time). A 4,000 sample (2 ms) pre-trigger interval was set. The reason for the longer pre-trigger interval is explained in Ulrich *et al.* [28]. Amplitude resolution is 16 bit. True zero time of the transmitter could be identified by electromagnetic crosstalk between transmitter and receiver cables, generating a small but easy to recognize impulse in the receiver data.

The laboratory contained other noise due to multiple experiments being run simultaneously. Due to a high noise lab environment and a lack of a power amplifier for the backpropagated transmitter signal, we apply an additional 2 kHz low-pass Butterworth filter on all data.

In order to test the stability of deconvolution for different values of the regularization parameter γ, we run the exact same experiment as for a single source described above and shown in Figure 4.1(b). Once the signal was recorded, we applied DC multiple times with different gamma values in order to generate the different signals to be backpropagated. We then ran the same workflow as shown in Figure 4.1(c) for each DC signal separate, recording the focused wavefield at the source location each time.

For multiple sources, we executed the workflow described above and shown in Figure 4.1(b) three times (once for every source). This was necessary because we did not have the equipment capabilities in this laboratory to generate a source function at all three source locations at different onset times. We recorded these three generated wavefields separately and then superimposed them. Due to the experiment being run separately three times, each recorded signal was normalized independently. This caused our recorded signals for all three sources to vary between amplitudes of -1 and 1. Thus, it destroyed the relative amplitude variation one would expect for three different sources at different locations and orientations. Once superimposed, TR or DC was applied and we carried out the same back propagation workflow as shown in Figure 4.1(c). During the backpropagation, one restores the relative amplitudes in the focus achieved because of reciprocity.

4.4 Single Source Experiment

The purpose of this experiment is to study the capabilities of TR and DC to focus the measured waveforms at a point in both space and time. The experiment began with propagating a defined 60 kHz source function from the embedded source towards the external receiver. The receiver's direction of measurement was perpendicular to the direction of source emission. Once our wave field was recorded at the single receiver, TR or DC was applied to calculate the back propagating signals.

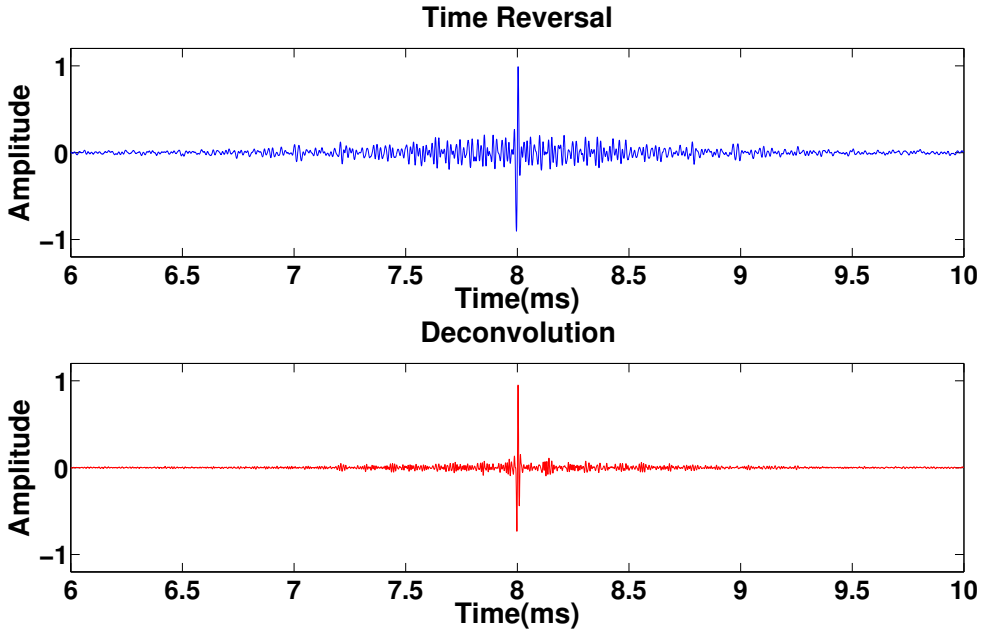

Figure 4.2: Normalized temporal focus measured at the embedded source location using (top panel) Time Reversal, and (bottom panel) Deconvolution for a single source and single receiver set up.

For a single source, deconvolution ideally achieves an improved temporal focus. This is due to there being a single term in the denominator as shown in Eq. 4.5, which leads to the following,

$$g(\omega)G(\omega) \approx \frac{G(\omega)G^*(\omega)S^*(\omega)}{|G(\omega)S(\omega)|^2 + \epsilon} \approx \frac{1}{S(\omega)}, \tag{4.7}$$

where $G(\omega)$ represents the Green's function describing the propagation between source and receiver, $S(\omega)$ represent the source function in the frequency domain, and $g(\omega)$ the signal we are trying to solve for with deconvolution. Equation. 4.6 should approach $1/S(\omega)$ as ϵ approaches 0. Therefore, the focus achieved using deconvolution approaches an optimal reconstruction of the inverse of the source function and not necessarily a Dirac delta function. When the source function is a delta function, $S(\omega)$ is constant, this leads to a delta function at the focal point.

The DC and TR signals were then backpropagated from the transducer on the surface of the block into the same medium and recorded at the original source location transducer. Figure 4.2 shows the refocused waves recorded at the source location where Figure 4.2 (a) is the temporal focus achieved using TR while Figure 4.2 (b) represents the temporal focus achieved using the DC calculated signal. The temporal focus achieved using TR has significant side-lobes away from the time of focus; the temporal focus achieved using DC has suppressed most of these side-lobes and was able to produce a better focus. In order to quantify this improvement, we calculate the amount of energy in a .02 ms window around the time of focus compared to the total energy of the signal. The temporal focus achieved using TR only had 41% of the total energy within this window while DC's temporal focus had 80% of the total energy within this window. Thus, DC is able to generate a significantly better temporal focus than TR. Our source function used wasn't a Dirac delta function but deconvolution still improved the focus significantly as it improved the reconstruction of our source function. Once we had shown that deconvolution was able to improve the focus at a point in both space and time, we continued our experimental studies to investigate the robust nature of deconvolution.

4.5 Regularizing the Deconvolution

The purpose of this experiment was to study the robust nature of DC by changing the location of the receiver and investigating the effect of regularizing the deconvolution through the parameter ϵ used in equation 4.5. This experiment started the same way as our previous single source experiment. We first propagated a defined 60 kHz source function from the embedded source towards the external receiver. For this experiment, the receiver's direction of measurement was parallel to the direction of source emission. The recorded signal was then deconvolved using various values of γ which was the constant scalar number used to characterize the regularization term ϵ defined in equation 4.6. These calculated deconvolved signals were propagated back into the medium from the receiver location and recorded at the source transducer.

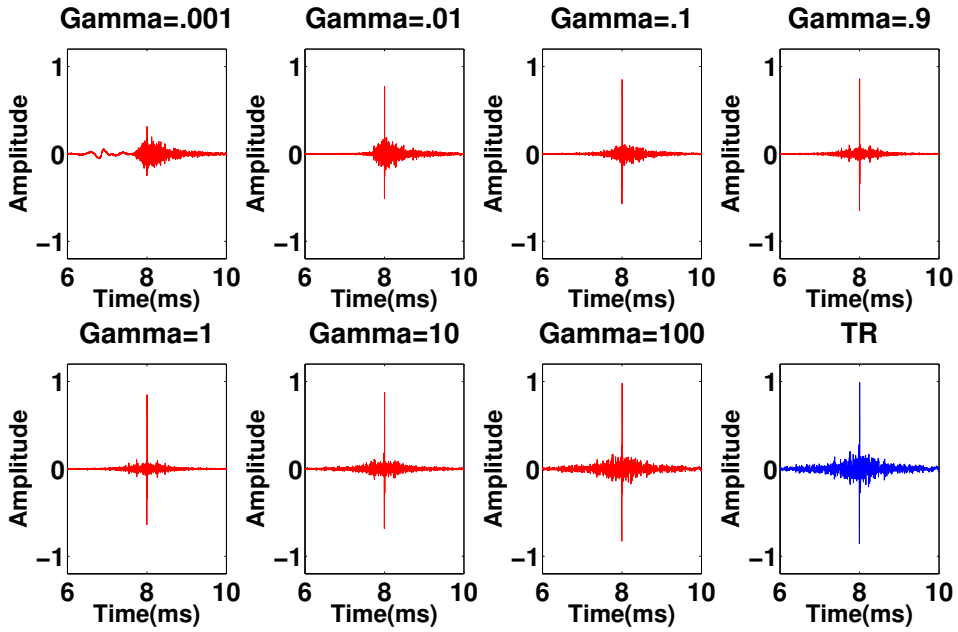

Figure 4.3: Normalized temporal focus measured at the embedded source location using different values for γ in the deconvolution (shown in red) and time reversal(shown in blue)

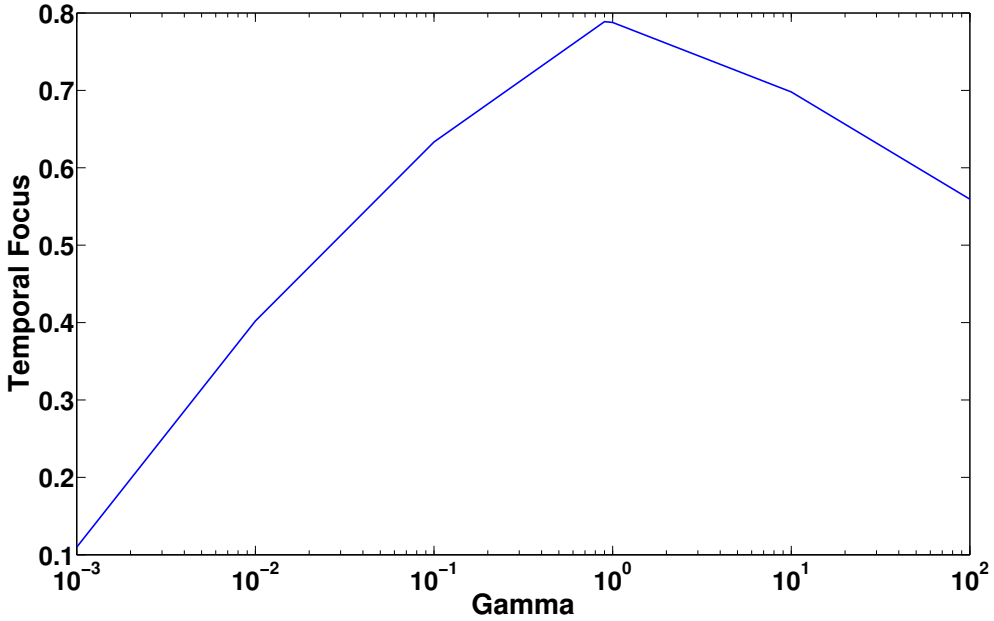

Figure 4.4: The temporal focus, defined as the amount of energy in a .02 ms window around the time of focus compared to the total energy of the signal, as function of γ. High temporal focus indicates most of the energy is compressed at the time of focus.

Theoretically, we would expect the focused wavefield to contain significant amount of noise at low γ values. As γ increases, the temporal focus is expected to improve because we reduce the effect of noise and force our signal to generate a better approximate Dirac delta function focus. However, if γ becomes too large, one approaches the temporal focus achieved using TR. This can be seen as follows: For time reversal, $g(t) = R(-t)$, therefore, $g(\omega) = R^*(\omega)$. If γ is large, ϵ becomes large in the sense that $\epsilon >> |R(\omega)|^2$, and equation 4.5 reduces to

$$g(\omega) \approx \frac{1}{\epsilon} G(\omega)^* S(\omega)^* = \frac{1}{\epsilon} R^*(\omega),$$

which implies that our deconvolved signal is just a scaled version of the time reversed signal.

Figure 4.3 shows the normalized focused wavefield at the source location for TR and DC for different values of γ. For this experiment, we quantified the temporal focus the same way as the previous experiment with the identical window size of .02 ms used. The optimal DC's temporal focus was 79% (for a gamma value of 0.9) while TR had a temporal focus of 47%. We would not expect to see the exact same temporal focusing numbers as in our single source experiment because we changed the direction of displacement we record and the distance between the source and receiver.

Figure 4.4 highlights the effect of gamma by showing the temporal focus as a function of γ. If γ becomes small, the temporal focus achieved decreases. However, as γ becomes large, the temporal focus approaches TR's temporal focus of 47%. The experiment showed that the optimal value to be $\gamma = 0.9$. However, even for different γ values, one still achieves some form of a temporal focus as shown in Figure 4.3.

4.6 Multi Source Experiment

The purpose of this experiment was to study the effect of multiple sources when using deconvolution. We began by emitting the same 60kHz source function from different source transducers within the concrete block at different onset times. The experiment was repeated

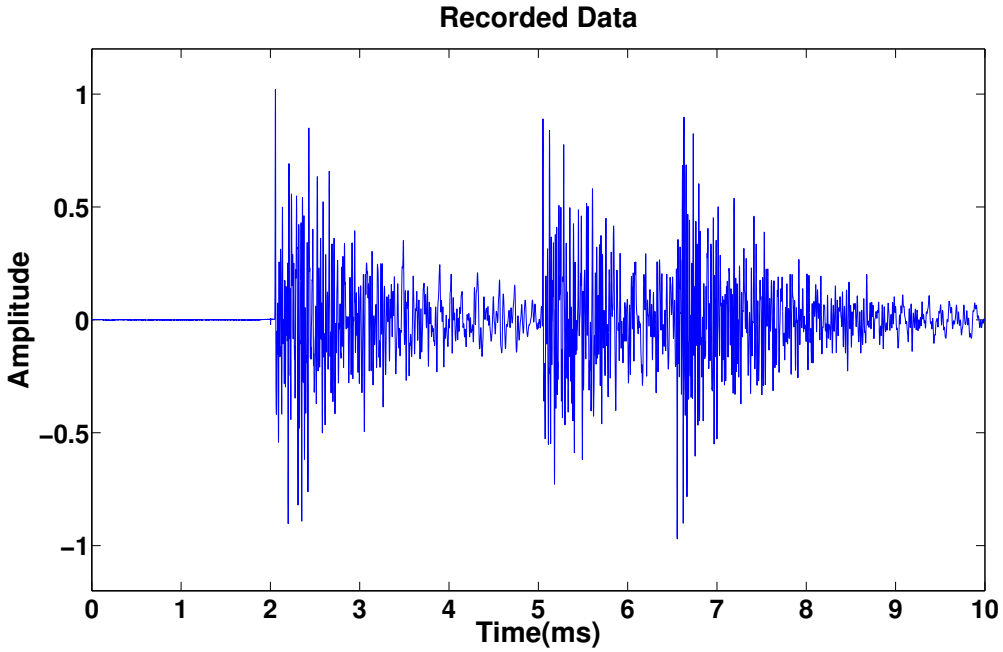

Figure 4.5: Recorded scattered waveforms at the receiver location due to three source wavefields being emitted at different times.

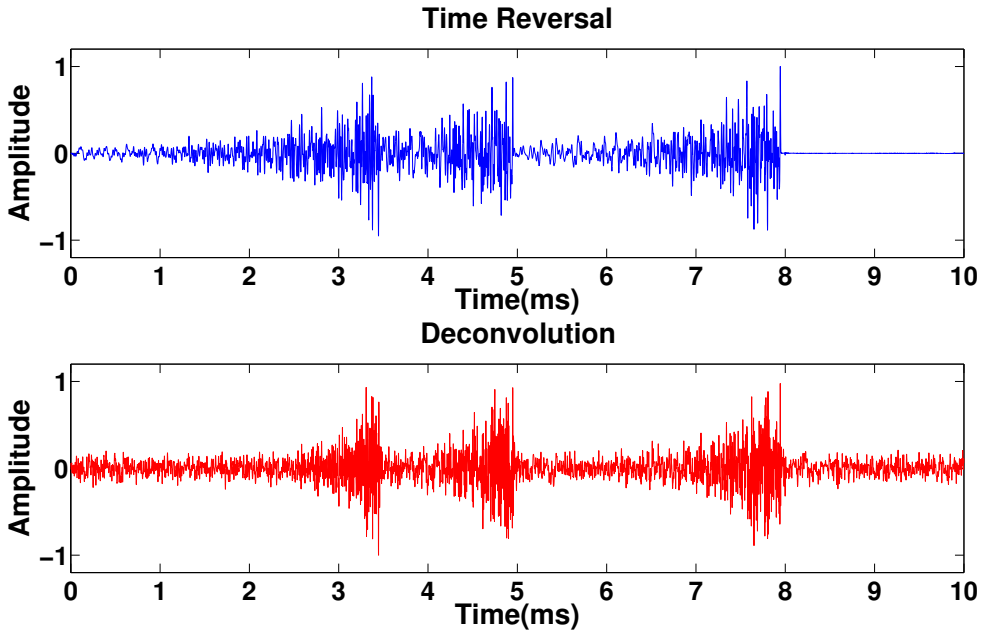

Figure 4.6: Back propagation signals calculated using Time Reversal(top panel) and Deconvolution(bottom panel). These signals are backpropagated into the medium for the multi-source experiment.

three times to record each source wavefield separately which normalized the recorded signals independently. The employed normalization caused our signals for all three sources to vary between amplitudes of -1 and 1. The three recorded wavefields due to the three sources were then superimposed before TR or DC was applied. Figure 4.5 shows the superimposed wavefield. Note the complexity of the wavefield due to scattering within the concrete sample. Due to the complicated nature of the recorded signal, one can assume that the cross-correlation of each source wave field is negligible:

$$G_i G_j^* \approx 0 \text{ for } i \neq j \tag{4.8}$$

where G_i for $i = 1, 2, 3$ is the Green's function characterizing the source wavefield for source 1, 2, or 3. Equation 4.8 is crucial in explaining why deconvolution is stable for multiple sources.

We apply time reversal and deconvolution to the superimposed signal consisting of the three source wavefields to generate our TR and DC signals shown in Figure 4.6. Deconvolution's signal differs from time reversal signal in its acausal nature, due to our pre-trigger time, where DC adds information past 8 ms while TR has zero amplitude after 8 ms. Additionally, the three different source wavefields are still clearly visible in the DC signal. Below, we demonstrate why deconvolution is able to focus the wavefield due to multiple source at each source location.

If there are three sources, the recorded signal in the frequency domain is given by

$$R(\omega) = G_1 S_1 + G_2 S_2 + G_3 S_3,$$

where $R(\omega)$ is the recorded signal in the frequency domain, and the subscripts indicate the source transducer used. The inverse signal obtained by deconvolution is given by

$$D_t(\omega) = \frac{1}{G_1 S_1 + G_2 S_2 + G_3 S_3} = \frac{1}{(G_1 S_1 + G_2 S_2 + G_3 S_3)} \frac{(G_1 S_1 + G_2 S_2 + G_3 S_3)^*}{(G_1 S_1 + G_2 S_2 + G_3 S_3)^*}.$$

We simplify the above solution and add the regulation term $\epsilon = \gamma$ mean$(|R(\omega)|^2)$ to get,

$$D_t(\omega) = \frac{(G_1S_1 + G_2S_2 + G_3S_3)^*}{|G_1S_1|^2 + |G_2S_2|^2 + |G_3S_3|^2 + \text{Crosstalk} + \epsilon}, \tag{4.9}$$

where Crosstalk$= G_1S_1G_2^*S_2^* + G_1S_1G_3^*S_3^* + G_2S_2G_1^*S_1^* + G_2S_2G_3^*S_3^* + G_3S_3G_1^*S_1^* + G_3S_3G_2^*S_2^*$, and $D_t(\omega)$ represents the deconvolved signal when the recorded signal contains three source wavefields.

If we recorded each sources' wavefield separate and applied deconvolution first before the superposition of the wavefields, we would get:

$$D_s(\omega) = \frac{(G_1S_1)^*}{|G_1S_1|^2 + \epsilon_1} + \frac{(G_2S_2)^*}{|G_2S_2|^2 + \epsilon_2} + \frac{(G_3S_3)^*}{|G_3S_3|^2 + \epsilon_3}, \tag{4.10}$$

where $D_s(\omega)$ represents the deconvolved signal when deconvolution is applied before superposition. One might expect that for a real scenario, where multiple sources are present, deconvolution would break down due to the influence of crosstalk. Because the recorded wavefields generated by each source are extremely complex, as shown in Figure 4.5, terms such as $G_1G_2^*$ are small (equation 4.8). Therefore, the influence of the crosstalk terms is minimal and we can assume it vanishes. This provides us with the following solution that relates $D_s(\omega)$ to $D_t(\omega)$,

$$D_s(\omega) = \frac{(G_1S_1)^*}{|G_1S_1|^2 + \epsilon_1} + \frac{(G_2S_2)^*}{|G_2S_2|^2 + \epsilon_2} + \frac{(G_3S_3)^*}{|G_3S_3|^2 + \epsilon_3} \approx 3\frac{(G_1S_1 + G_2S_2 + G_3S_3)^*}{|G_1S_1|^2 + |G_2S_2|^2 + |G_3S_3|^2 + \epsilon} = 3D_t(\omega), \tag{4.11}$$

where we assume $|G_1S_1| \approx |G_2S_2| \approx |G_3S_3|$.

Figure 4.7 shows that the approximation (4.11) holds. Figure 4.7 shows that after normalizing $D_s(t)$ and $D_t(t)$, one can note that there does not seem to be a obvious difference between $D_s(t)$ and $D_t(t)$. Thus, the crosstalk term may be ignored and deconvolution is stable and able to focus the wavefield due to multiple sources at each source location. We were able to do this calculation because we recorded each source wavefield separately.

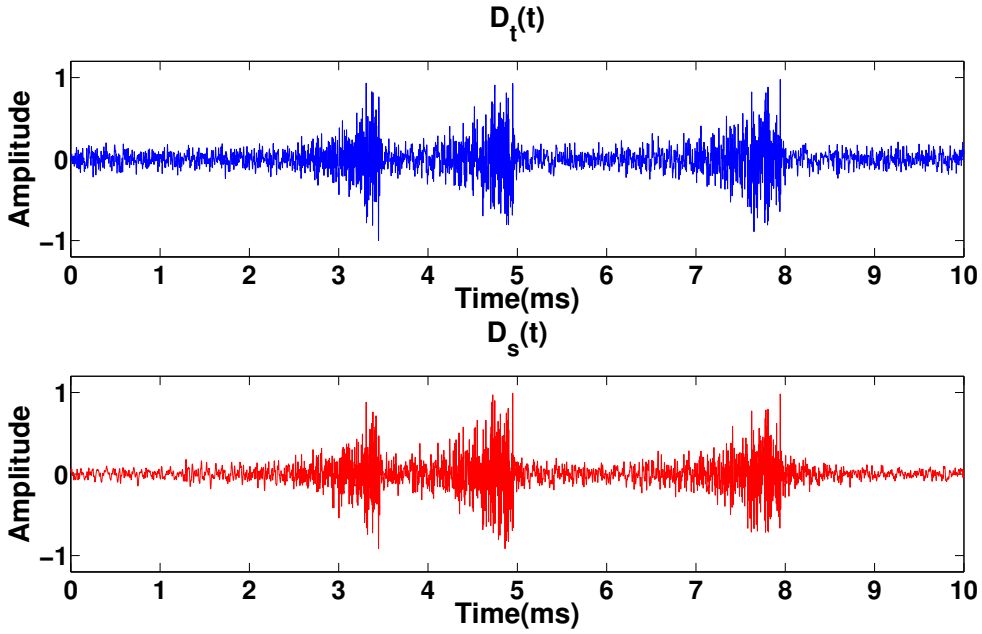

Figure 4.7: Comparison of deconvolution signal calculation. Top panel shows the DC signal after applying deconvolution to the superposition of the three recorded wavefields $D_t(t)$. Bottom panel shows the DC signal after applying deconvolution to the three recorded signals before adding them to each other $D_s(t)$. All signals are normalized.

In order to keep the experiment realistic, we back propagated the DC signal which was calculated after the superposition of the three separate wavefields. Figure 4.6 shows the wavefields calculated using TR and DC which are propagated back into the medium from the receiver location. We then used the transducers within the concrete block as our receivers. Figure 4.8 shows the focused wavefields at each of the three sources for TR, shown in the top panels, versus DC, shown in the bottom panels. For sources 1 and 2, deconvolution compresses the sidelobes substantially better than TR. However, for source 3, deconvolution does not significantly improve the focus compared to time reversal.

The orientation of our sources is an important factor. Source 1 and 2 were oriented perpendicular to Source 3, and as a result the recorded waves excited by Source 3 are stronger than those excited by Source 1 and 2. However, as previously stated, we ran each source wavefield propagation separately which normalized the recorded signals independently

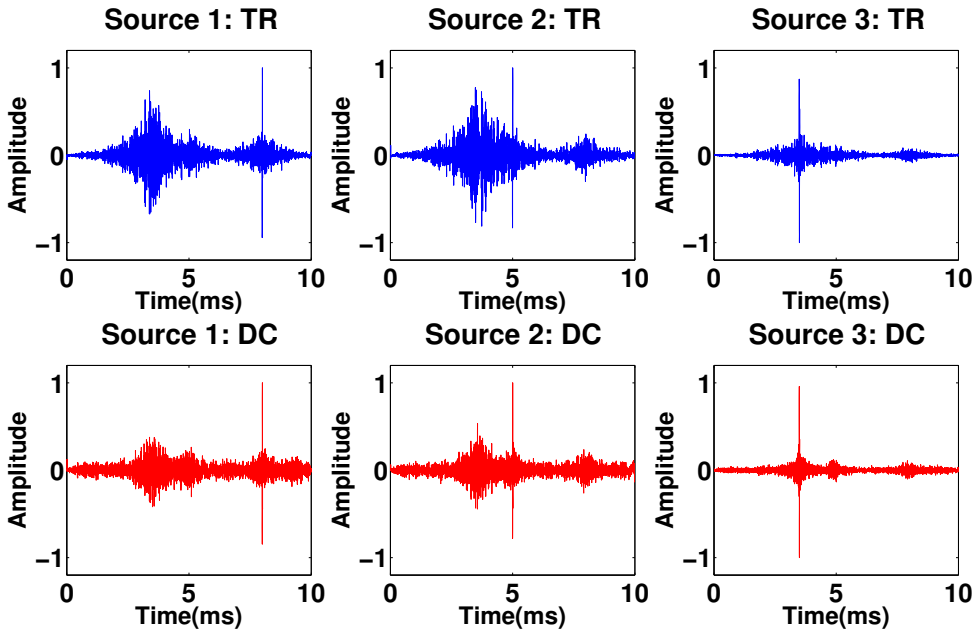

Figure 4.8: Temporal focus measured at the three embedded source location using (top panels) Time Reversal's signal, and (bottom panels) Deconvolution's $D_t(t)$ signal and back propagating it from the transducer on the surface of the concrete sample.

causing the amplitudes of each recorded source wavefield to vary between amplitudes of -1 and 1. Thus, our superimposed signal shown in Figure 4.5 does not show a higher amplitude for the source 3 wavefield. However, when we back propagate our TR and DC wavefield, due to reciprocity, the source 3 wavefield focus will have a higher amplitude. This causes the crosstalk terms to be negligible for the source 3 focus because,

$$|G_3(\omega)| >> |G_1(\omega)| \text{ and } |G_3(\omega)| >> |G_2(\omega)|. \tag{4.12}$$

Under these conditions, eqn. 4.9 reduces to,

$$D_t(\omega) \approx \frac{(G_3 S_3)^*}{|G_3 S_3|^2 + \epsilon}, \tag{4.13}$$

which is what we had before.

Figure 4.8 shows that equation 4.12 holds because, for source 3, the focus has significantly higher relative amplitude than the crosstalk terms. For source 1 and 2, the maximum amplitude of the crosstalk is closer to the maximum amplitude of its focus.

In conclusion, for multiple sources, deconvolution is able to focus the energy at the source location at the correct time. It is arguable whether time reversal or deconvolution is better in generating a focus. However, the experiment does prove the robust nature of DC in that it will not fail under the condition of multiple sources.

4.7 Conclusion

We have introduced in an experimental study a simple though robust method for determining the optimal signal for backpropagation such that one gets an improved temporal focus at the source location. Deconvolution was shown to have an optimal regularization parameter, γ, for improved temporal focusing. If one increases γ, the temporal focus approaches that of TR; if one decreases γ, one increases the effect of noise and the temporal focus decreases dramatically. However, Figure 4.3shows that one still attains a focus even for different values of γ. Additionally, deconvolution does not break down when there are multiple source wavefields being propagated. This is due to the influence of the crosstalk terms being minimal. Thus, deconvolution has a robust nature comparable to that of time reversal while having the potential to dramatically improve the focus. In conclusion, the simple and robust nature of deconvolution allows it to be implement as a preprocessing step in order to improve focusing at the source location.

CHAPTER 5

LOCATING A MICROSEISMIC EVENT USING DECONVOLUTION

We demonstrate a technique to enhance the ability of imaging the location of a microseismic event by improving both spatial and temporal focusing. The technique improves locating a microseismic event in a velocity model for which the interface boundaries are approximate but where it has the correct mean slowness. Our method designs a signal to be rebroadcasted from the receivers, using only the waves recorded at each receiver, such that the wave field has an optimal temporal focus at the source location. Additionally, this procedure leads to an improved spatial focus of the wave field. The numerical test shown include additive noise. This proposed technique only involves a simple preprocessing step to the recorded data and its cost is hence negligible compared to the total cost of microseismic imaging.

5.1 Introduction

Microseismic events occur naturally or as a result of production or hydraulic stimulation [5, 6]. Clusters of microseismic events delineate faults and the formation of fractures and can indicate new or reactivating regions of failure. As hydraulic fracturing is becoming increasingly widespread, operators are aiming to monitor the induced events in order to characterize a reservoir. This has led to a need from the industry to develop more accurate ways of locating and monitoring microseismic events [7].

A standard processing method is based on picking arrival times of P and S waves. This process is, however, difficult when significant noise is present in the data and thus can require extensive user interaction [34–38]. An alternative approach to locate events is by imaging the time reversed signal to focus microseismic signal at the source position [39–42]. The advantage of imaging the time reversed signal is that it does not require picking of arrival

times, this is of particular importance for noisy data. In the imaging approach, one usually uses time reversal to focus the recorded waves at the source location in space and time [39].

If one time reverses the waves at every point in space, the wavefield will focus onto the original source location. If, however, the wavefield is sampled at only a limited number of locations, then it is not obvious that time reversal is the optimal way to focus energy on the original source. Much research has been carried out on focusing sparsely sampled wavefields [2, 4, 8–16, 43]. In this letter, we explore a simple extension to time reversal, based on deconvolution, as previously derived by [28], to improve our imaging for locating a microseismic event. This method is a robust, though simplified, version of the inverse filter [8, 9, 12]. It calculates a signal to be rebroadcast from the receiver such that the output at the focal location becomes an approximate delta function $\delta(t)$ and uses only the recorded signals at each receiver.

As with all imaging methods, reverse time imaging is unable to locate the microseismic event to a point location when the velocity model isn't the true velocity model or the aperture is poor; it causes the spatial image to defocus. We propagate the deconvolved waveforms through a smoothed version of the true slowness model. The local average of the slowness for this incorrect velocity model is equal to local average slowness of the true velocity model.

5.2 Theory-Deconvolution

Time reversal states that for a given recorded impulse response, a simple reversal in time of that signal followed by rebroadcasting the reversed signal from the receivers focuses an impulsive function $\delta(t)$ at the source location,

$$f(t) = \sum_i r_i(t) \star r_i(-t) \approx \delta(t) \tag{5.1}$$

where $\star$ denotes a convolution operator, $r_i(t)$ is the recorded impulse response at receiver i, and $r_i(-t)$ its time reversed counterpart. Equation (5.1) states that the autocorrelation of the recorded signal is ideally equal to a delta function. In practice, however, time reversal (TR) experiments are unable to recreate a true delta function focus as one or more condi-

tions necessary to satisfy equation (5.1) are typically violated. For example, if attenuation is present in the medium, time reversal (TR) can not create a true delta function focus. Additionally, if the aperture is finite, TR experiments can not create a true delta function focus. Given these limitations, we introduce deconvolution to achieve a more impulsive focusing in time.

Let us assume that time reversal is not able to create a Dirac delta focus after rebroadcasting the time reversed impulse response. We aim to find a signal such that after rebroadcasting we get a temporal focus that is approximately equal to a Dirac delta function. Thus, we change equation (5.1) to

$$f(t) = \sum_i r_i(t) \star g_i(t) \approx \delta(t) \ , \tag{5.2}$$

where $f(t)$ is the back propagated signal at the source, $r_i(t)$ is the recorded impulse response at receiver i, and $g_i(t)$ is the signal that is back propagated to the source from receiver i. We determine the backpropogated signal $g_i(t)$ from the requirement that the right hand side of the equation (5.2) approximates a delta function as well as possible. In the frequency domain, this corresponds to the requirement,

$$\sum_i r_i(\omega) g_i(\omega) \approx 1 \ . \tag{5.3}$$

This condition defines the signal that optimizes the temporal focus at the source location. Equation (5.3), applied to each receiver states that

$$g_i(\omega) = \frac{1}{r_i(\omega)} \approx \frac{r_i^*(\omega)}{|r_i(\omega)|^2 + \epsilon}, \tag{5.4}$$

where $r(\omega)r^*(\omega) = |r(\omega)|^2$. We introduce a regularization parameter ϵ to stabilize the deconvolution that satisfies

$$\epsilon = \gamma \times mean(|r_i(\omega)|^2) \ . \tag{5.5}$$

where γ is a constant, which is sometimes referred to as the waterlevel parameter [24], and the mean is calculated for each receiver over the frequencies for which the power spectrum differs significantly from zero. For small values of γ, the deconvolution may be sensitive to

additive noise, whereas for larger values of γ the deconvolution reduces to time reversal. We choose the value of γ by maximizing the energy in a 80m by 80m region around the source. This process is similar to the time-domain procedure developed by [24]. We used a value of $\gamma = 0.272$ in all experiments shown. An inverse Fourier transform takes $g(\omega)$ back into the time domain. One can then directly rebroadcast $g(t)$ and does not have to apply a time reversal operation on $g(t)$.

5.3 Microseismic event locating

The purpose of this study is to optimize microseismic event location using deconvolution. We use the velocity model shown in the top panel of Figure 5.1 to propagate the source wavefield to the receivers. The model consists of horizontally continuous layers whose velocities range from approximately 5 km/s to 6.6 km/s. In practice, one does not know the true velocity model. For this reason, we used the smoothed velocity model, shown in the bottom panel of Figure 5.1, for the back propagation. The velocity model is smoothed by using a two-dimensional triangle smoothing with a smoothing radius of .185 km in the z, and x direction [44]. This smoothed velocity model has the same mean slowness as the correct velocity model.

The location of the source is at $(x, z) = (0.51 \text{ km}, 2.68 \text{ km})$. The source wavelet is a Ricker wavelet with dominant frequency of 150 Hz. We use 56 receivers distributed over 2 vertical boreholes in our model. The x-locations of the receiver boreholes are 0.74 km and 0.88 km. The receivers range from a depth of 2.36 km to 2.86 km with a spacing of 18.5 m.

We find the focus time without knowing the triggering time. We do so by rebroadcasting our calculated inverse signal, producing an image every time step, and then calculate the energy of the spatial focus in a region around the source location until it reaches a maximum. In order to make the numerical simulation more realistic, we added noise to our recorded data at the receivers before running the time reversal or deconvolution process. Thus, both processes deal with the same noise. The additive noise only contains frequencies within the bandwidth of the data. The energy ratio of the signal to noise, defined as the ratio

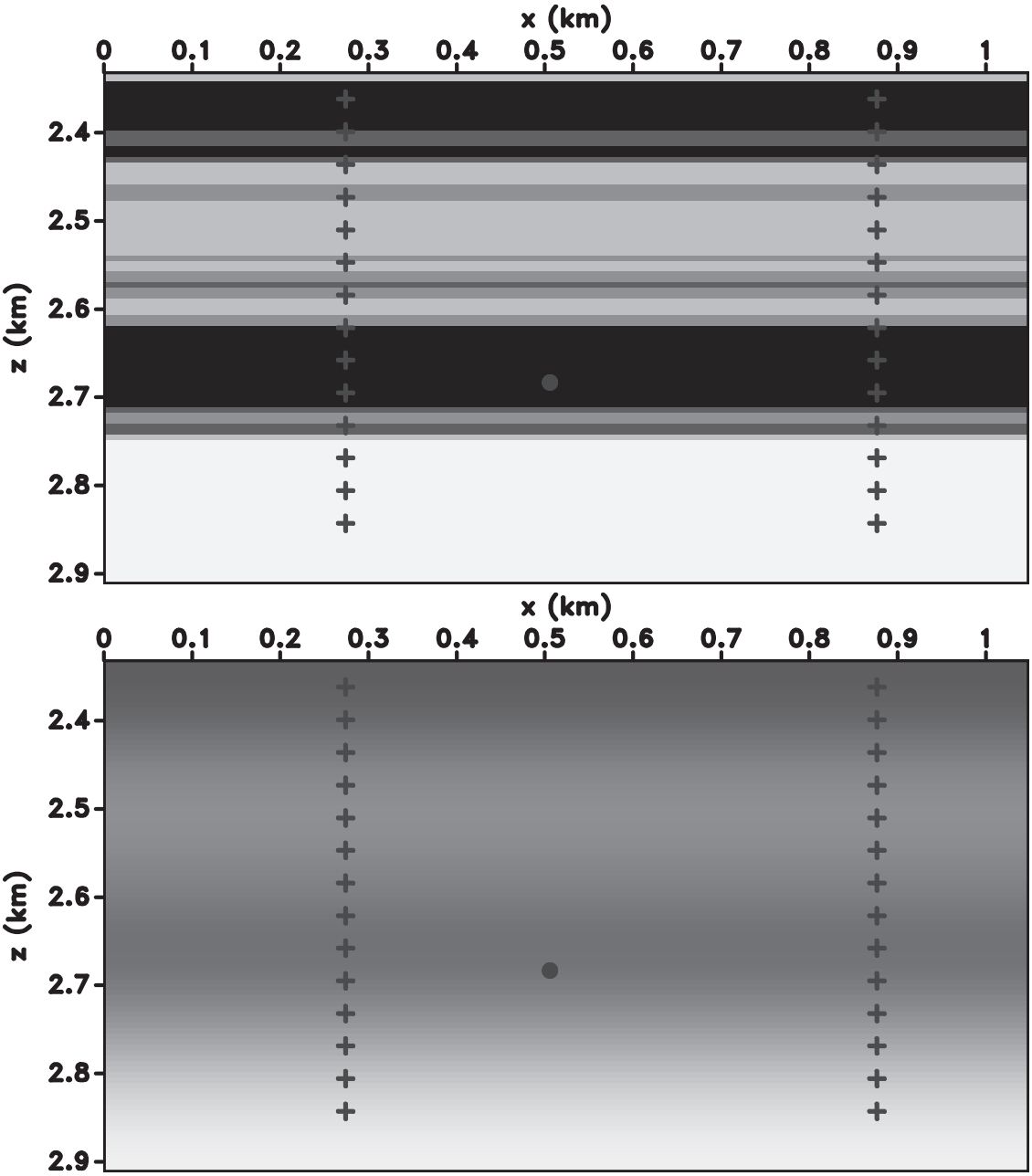

Figure 5.1: Velocity models of the numerical experiment. Top panel indicates the correct velocity model and represents the velocity model used to propagate the source wavefield through the medium. Bottom panel indicates the smoothed velocity model with correct mean slowness. This model is used for back propagation of the time reversed signal and optimized inverse signal. The plus symbols represent the receivers, the circular dot represents the source.

of the sum of the absolute values of the signal and noise squared, is equal to 0.89. The noise-contaminated data thus produced are shown in Figure 5.2.

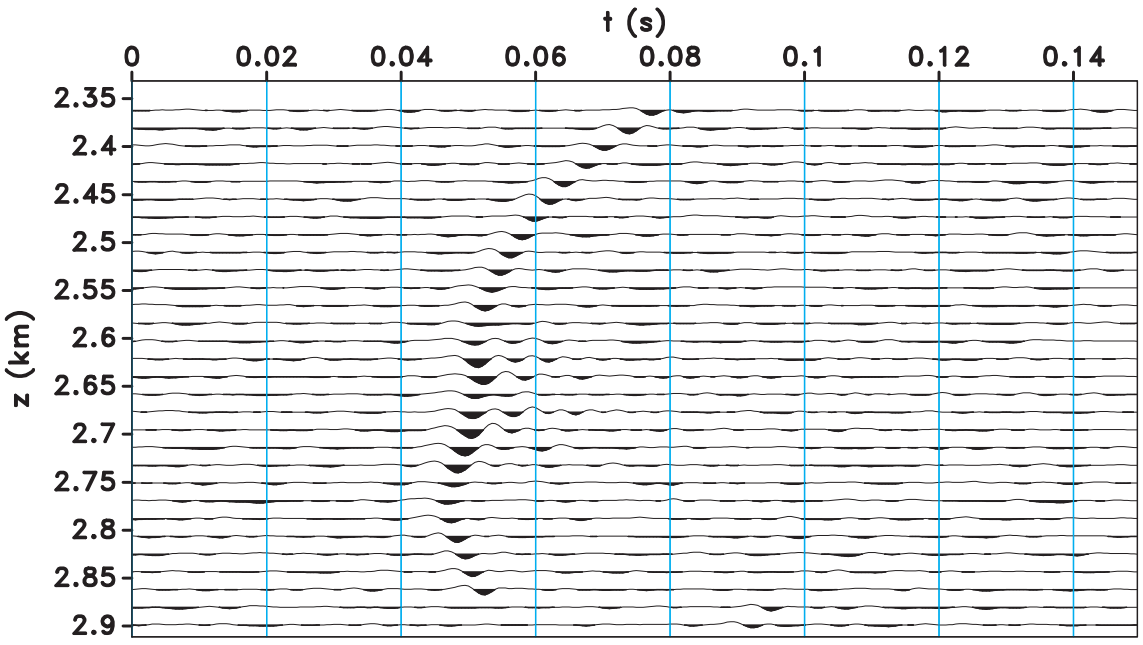

Figure 5.2: Wavefield excited by the source in Figure 5.1 after propagation through the true velocity model (top panel of Figure 5.1). Bandlimited noise is added to the data, the signal to noise ratio is .89.

As shown in Figure 5.3, deconvolution produces better spatial focusing than does time reversal. This allows one to find the location of the microseismic event with higher accuracy. This is possible because deconvolution suppresses the temporal sidelobes of the refocused signal and thus compresses more of the wave energy into the focus at the event time ($t = 0$). In order to compare the spatial focusing of each method, we show in Figure 5.4(c) and (d) horizontal slices of the spatial image at the depth of the source at the time of the focus ($t = 0$). Figure 5.4(d) illustrates that deconvolution improves spatial focusing compared to simple time reversal (Figure 5.4(c)). We quantify this improved spatial focusing by computing the ratio of the energy near the focus and the total energy. Using a window centered at the source location with a width of 20 m, we calculated the energy of the focus. Dividing the energy of the focus by the total energy gives us the spatial energy ratio of the focus.

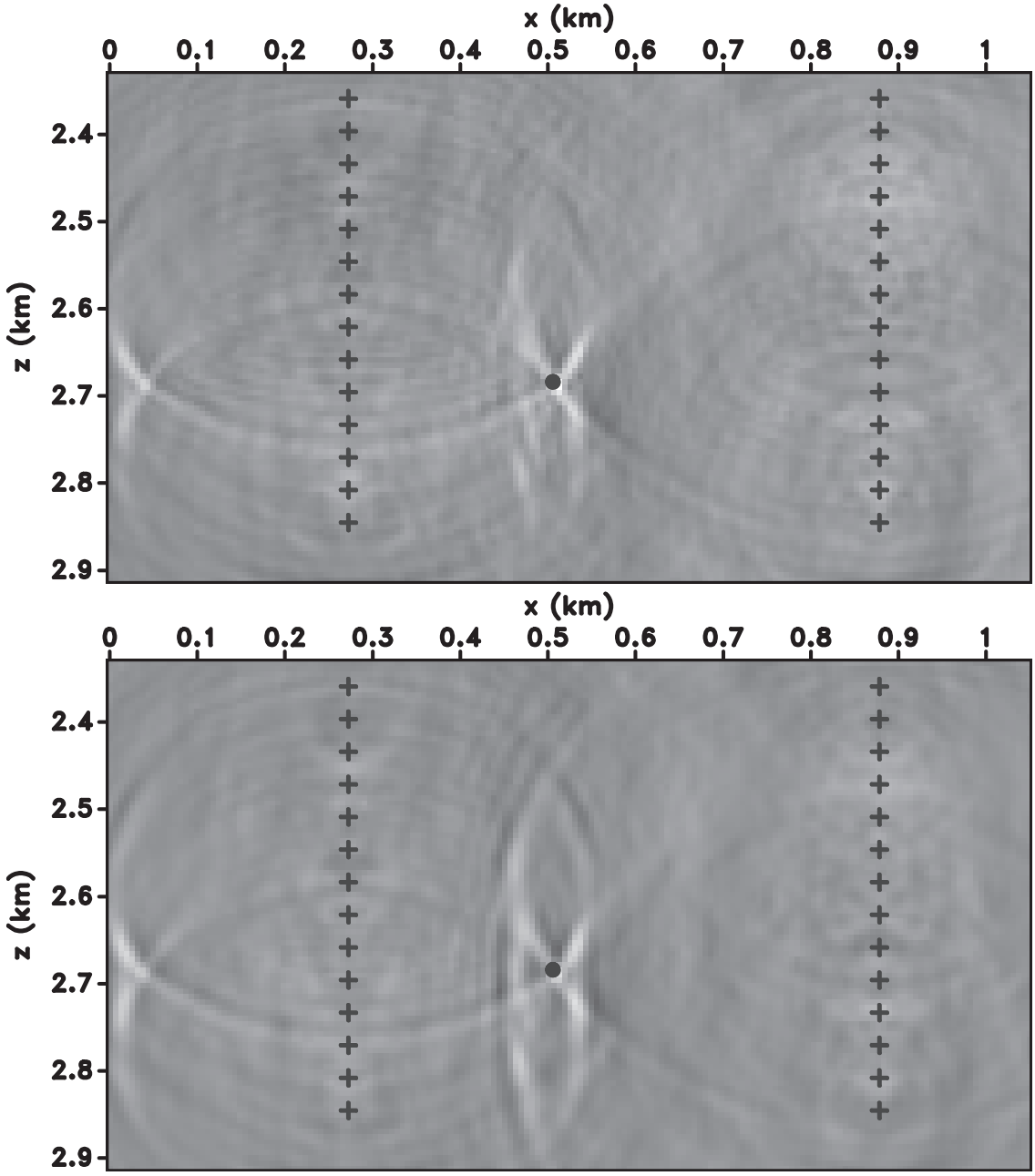

Figure 5.3: Wavefield $p(\mathbf{x}, t = 0)$ for deconvolution (top panel) and time reversal (bottom panel). The plus symbols represent the receivers, the circular dot represents the source. These images were created by back propagating the time reversed and inverse optimized signal through the incorrect velocity model (bottom panel of Figure 5.1).

Deconvolution yields a spatial energy ratio of 48% while time reversal has a spatial energy ratio of only 31%, which indicates quantitatively that deconvolution improves the spatial focus of a microseismic event.

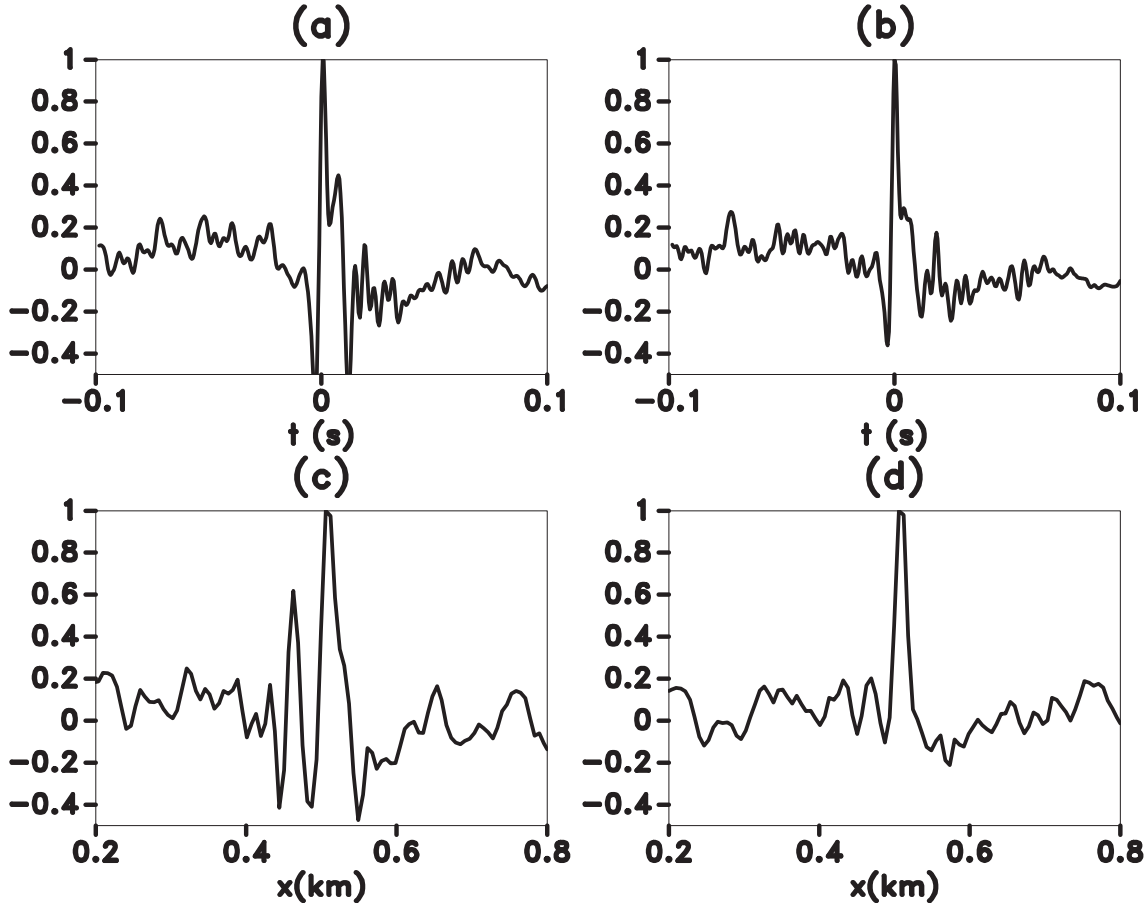

Figure 5.4: Temporal and spatial focused images produced by back propagating the calculated time reversed signals using time reversal and deconvolution for vertical borehole array. (a) Temporal focus at the source location obtained for time reversal, (b) Temporal focus at the source location obtained for deconvolution, (c) Horizontal cross section through the source depth at $t = 0$ obtained for time reversal, (d) Horizontal cross section through the source depth at $t = 0$ obtained for deconvolution.

We next consider temporal focusing. Figure 5.4(a) and (b) show improved temporal focusing for the deconvolution method compared to time reversal. We quantify the temporal focusing by computing the ratio of the energy near focus and the total energy. Using a window centered at $t = 0s$ with width of $.003s$, we calculated the energy of the temporal

focus. Dividing this focused energy by the total energy gives us the temporal energy ratio of the focus. Deconvolution has a temporal energy ratio of 49% while time reversal has a temporal energy ratio of 40%. Thus, deconvolution improves temporal focusing.

In conclusion, deconvolution improves both temporal and spatial focusing for our model. This allows one to locate microseismic events with greater accuracy, even when the velocity model is not the true model and additive noise is present. Deconvolution improves spatial focusing even though the method we introduced is designed to improve temporal focus. It was shown by [28] that improved temporal focusing improves spatial focusing for the spherically symmetric part of the focused wave field..

5.4 Improved temporal focusing leads to improved spatial focusing

In this section, we show that better temporal focusing implies better spatial focusing for the spherical average of the focus. We begin by first considering the wave field near its focal spot at $r = 0$ and consider the medium to be locally homogeneous in that region. The solution of the Helmholtz equation in an acoustic, homogeneous medium can be written as

$$p(r, \theta, \varphi, \omega) = \sum_{l=0}^{\infty} \sum_{m=-l}^{m=l} a_{lm} j_l(kr) Y_{lm}(\theta, \varphi) \ , \tag{5.6}$$

see Table 8.2 of [27]. In this expression j_l denotes the spherical Bessel function, Y_{lm} the spherical harmonics, and $k = \omega/c$, where c is the wave speed. According to expressions (11.144) and (11.148) of [27], $j_l(0) = 0$ for $l \geq 1$ and $j_0(0) = 1$. This means that at the focal point $r = 0$ only the terms $l = m = 0$ contribute. Using $Y_{00} = 1/\sqrt{4\pi}$ (Table 12.3 of [27]), this means that at the focal point

$$p(r = 0, \theta, \varphi, \omega) = \frac{a_{00}}{\sqrt{4\pi}} \ . \tag{5.7}$$

The properties of the wave field at the focal point thus only depend on the coefficient a_{00}. Since the $l = m = 0$ component of the spherical harmonics expansion gives the spherically symmetric component of the wave field, the properties of the wave field at the focal point can only bear a relation to the spherically symmetric component of the wave field. The

properties of temporal focusing can thus be related to the spherically symmetric component of the spatial focusing only.

Because of this, we restrict ourselves to the spherically symmetric component ($l = m = 0$) of the wave field at the focal point. Using that $j_0(kr) = \sin(kr)/kr$, the spherically symmetric component of Eq. (5.6) is given by

$$p(r, \omega) = p_0 \, \frac{e^{-ikr} - e^{ikr}}{r} \, , \tag{5.8}$$

with $p_0 = -a_{00}/(2ik\sqrt{4\pi})$. The coefficient p_0 depends on frequency. Using the Fourier convention $f(t) = \int p_0(\omega) e^{-i\omega t} d\omega$, and using that $k = \omega/c$, Eq. (5.8) corresponds, in the time domain, to

$$p(r, t) = \frac{f(t + r/c) - f(t - r/c)}{r} \, . \tag{5.9}$$

In this equation, $f(t+r/c)$ denotes the wave that is incident on the focus, and $f(t-r/c)$ the outgoing wave once it has passed through the focus.The field at the focus follows by Taylor expanding $f(t \pm r/c)$ in r/c and taking the limit $r \to 0$, this gives

$$p(r = 0, t) = \frac{2}{c} f'(t) \, . \tag{5.10}$$

In this expression and the following, the prime denotes the time derivative. Equation (5.10) states that the wave field at the focus is the time derivative of the incoming wave field and provides the temporal properties of the focus.

In order to get the spatial properties, we consider the wavefield near the focal point at time $t = 0$. Setting $t = 0$ in Eq. (5.9), gives

$$p(r, t = 0) = \frac{f(r/c) - f(-r/c)}{r} \, . \tag{5.11}$$

Equation (5.11) states that the wave field at the time of focus is the difference between the incoming and outgoing wave and gives the spatial properties of the focus.

A improved temporal focus implies that $f'(t)$ is only nonzero for values of t close to $t = 0$. It follows from Eq. (5.11) that if that is the case, then $p(r, t = 0)$ is localized near $r = 0$. Note that if a constant was added to f when going from $f'(t)$ to $f(t)$, our conclusion would

not change because the constant would be subtracted and cancelled out in Eq. (5.11).

5.5 Conclusion

We have introduced a method that improves temporal focusing of a microseismic event. The method can be beneficial for locating a microseismic event because it also improves spatial focusing compared to the standard time reversal method. We have shown how this techniques improves the locating for a microseismic event using synthetic data contaminated with additive noise. The simplicity and robust nature of this method allows for a simple incorporation into existing reverse-time imaging methods. The cost of the deconvolution is minimal compared to running the finite difference model. Thus, it can be added as a preprocessing step without significant additional cost. Further research is being completed by us on extending this method to elastic waves excited by a double couple and point force sources.

CHAPTER 6

FOCUSING OF ELASTIC WAVES FOR MICROSEISMIC IMAGING

Microseismic events generate compressive waves and shear waves which can be recorded at receivers. We present a theory that shows how elastic P and S waves separately back-propagate to the original source location. These refocused P and S wavefields are free of singularities. We also demonstrate a technique that enhances the ability to image the spatial focus for each wave type using elastic waves. The improved spatial focus obtained is achieved in a velocity model for which the interface boundaries are approximate but where the mean slowness is correct. Deconvolution designs a signal to be rebroadcasted from the receivers, using only the waves recorded at each receiver, such that the wavefield has an optimal temporal focus at the source location. We demonstrate theoretically and numerically that improved temporal focusing of elastic waves leads to improved spatial focusing for each wave type. This proposed technique only involves a simple preprocessing step to the recorded data and its cost is hence negligible compared to the total cost of microseismic imaging.

6.1 Introduction

Due to hydraulic fracturing becoming a common practice for unconventional gas and oil fields, there has been an increased interest into the study of microseismic events. Clusters of microseismic events delineate faults and the formation of fractures, and can indicate new or reactivating regions of failure. These microseismic events can be generated naturally or as a result of hydraulic stimulation [5, 6]. Therefore, the petroleum industry desires to develop more accurate ways of locating, and monitoring microseismic events to potentially improve their relationship to production and completion data [7].

A common processing method to locate microseismic events or earthquakes is based on picking arrival times of the acoustic and shear waves. This process, however, is difficult to do accurately when significant noise is present in the data [34–38]. An alternative approach, which requires less user interaction and allows for more accuracy, is using time reversal to image the focus of the microseismic events or earthquakes at the source location [4, 39–42, 45, 46]. In this imaging approach, one uses time reversal to focus the recorded signal at the source location in both time and space. The advantage of time reversal is that it does not require picking of arrival times which is important when dealing with noisy data.

If one would time reverse the waves at every point in space, the wavefield will focus onto the original source location. If, however, the wavefield is sampled at only a limited number of locations, then it is not obvious that time reversal is the optimal way to focus energy on the original source. Much research has been carried out on focusing sparsely sampled wavefields [2, 4, 8–16, 43]. In this paper, we explore a simple extension to time reversal, based on deconvolution, as previously derived by [28]. We have shown earlier that deconvolution improves the locating of microseismic events in an acoustic medium [47]. We now demonstrate deconvolution's ability to improve the imaging of a microseismic event in an elastic medium. This method is a robust, though simplified, version of the inverse filter [8, 9, 12]. It calculates a signal to be rebroadcast from the receiver such that the output at the focal location becomes an approximate delta function $\delta(t)$ and uses only the recorded signals at each receiver.

As with all imaging methods, reverse time imaging is unable to locate the microseismic event to a point location when the velocity model used for the backpropagation differs from the true velocity model, or when the aperture is limited; it causes the spatial image to defocus. In the numerical example used for this paper, the aperture used is not perfect, thus, the wavefield is not known at every point in both time and space. Additionally, we complicate our model by back-propagating our wavefields not through the correct velocity model but through a smoothed version of the velocity model.

In this paper, we first derive a relationship between the temporal focus and the incoming wave for an elastic medium. The theory is used to show that improved temporal focusing leads to improved spatial focusing for each wave type due to different sources (explosive, point force, and double couple). We then show a numerical example in which a horizontal point force excites elastic waves.

6.2 Theory

In this section, we show that improved temporal focusing leads to improved spatial focusing for both P- and S- waves. We first consider a homogeneous elastic medium where either P, SV, or SH waves are incident on a focal point. According to expression (8.13) of [48], the elastic wavefield can be expressed as

$$\mathbf{u}(r,\theta,\varphi) = \sum_{lm} \left(U_l(r)\mathbf{R}_l^m(\theta,\varphi) + V_l(r)\mathbf{S}_l^m(\theta,\varphi) + W_l(r)\mathbf{T}_l^m(\theta,\varphi) \right) \ . \tag{6.1}$$

The vector spherical harmonics in equation 6.1 are given by

$$\mathbf{R}_l^m(\theta,\varphi) = Y_{lm}(\theta,\varphi)\hat{\mathbf{r}} \qquad (\mathrm{P}-\mathrm{waves}) \ , \tag{6.2}$$

$$\mathbf{S}_l^m(\theta,\varphi) = \frac{1}{\sqrt{l(l+1)}} \left(\frac{\partial Y_{lm}(\theta,\varphi)}{\partial\theta}\hat{\theta} + \frac{1}{\sin\theta}\frac{\partial Y_{lm}(\theta,\varphi)}{\partial\varphi}\hat{\varphi} \right) \qquad (\mathrm{SV}-\mathrm{waves}) \ , \tag{6.3}$$

$$\mathbf{T}_l^m(\theta,\varphi) = \frac{1}{\sqrt{l(l+1)}} \left(\frac{1}{\sin\theta}\frac{\partial Y_{lm}(\theta,\varphi)}{\partial\varphi}\hat{\theta} - \frac{\partial Y_{lm}(\theta,\varphi)}{\partial\theta}\hat{\varphi} \right) \qquad (\mathrm{SH}-\mathrm{waves}) \ , \tag{6.4}$$

where $Y_{lm}(\theta,\varphi)$ denote the spherical harmonics. The radial functions $U_l(r)$, $V_l(r)$ and $W_l(r)$ are spherical Bessel functions or spherical Hankel functions which satisfy equation (8.6) of [48].

We consider the case of an incoming wave that, at a large distance from the focal point $\vec{r} = 0$, is given by $f_l(t + r/c)/r$. We study the properties of this incoming wave at the focus for every angular degree l separately. For a perfect aperture, the angular degree l describes an explosive source when $l = 0$, a point force when $l = 1$, and a double-couple source when $l = 2$. Since there is no source at the location $\vec{r} = 0$, the solution is finite and is therefore

given by spherical Hankel functions j_l :

$$U_l(r) \propto j_l(kr) \quad \text{where} \quad k = \omega/\alpha \ , \tag{6.5}$$

with α representing the P-wave velocity, and

$$V_l(r) \quad \text{and} \quad W_l(r) \propto j_l(kr) \quad \text{with} \quad k = \omega/\beta \ , \tag{6.6}$$

where β the S-wave velocity. Thus, the radial variation of the wavefield is proportional to $j_l(kr)$, with k the wavenumber of the wave type under consideration. In the following, we study wavefields with radial dependence $j_l(kr)$ and denote the wavenumber as

$$k = \omega/c \ , \tag{6.7}$$

where c is the appropriate wave velocity (α or β depending on the wave type). It is understood that the total wavefield follows by multiplying with the appropriate vector spherical harmonic as given in expressions (6.2)-(6.4). The radial dependence of the wavefield in the frequency domain, therefore, is given by

$$U_l(r, \omega) = A_l(\omega) j_l(kr) \ , \tag{6.8}$$

where $A_l(\omega)$ is a Fourier coefficient.

Using the Fourier convention $f(t) = \int F(\omega) e^{-i\omega t} d\omega$, the wavefield in the time domain is given by

$$u_l(r, t) = \int A_l(\omega) j_l(kr) e^{-i\omega t} d\omega \ . \tag{6.9}$$

The waves impinging on the focus are determined by the incoming waves. For large radius r, the incoming waves can be written as

$$u_l^{inc}(r, t) = \frac{f_l(t + r/c)}{r} \quad \text{as} \quad r \to \infty \ . \tag{6.10}$$

We show in the appendix that the total wavefield is given for all values of r by,

$$u_l(r, t) = (-i)^l \, \frac{2}{c} \int (-i\omega) F_l(\omega) j_l(kr) e^{-i\omega t} d\omega \ , \tag{6.11}$$

where $F_l(\omega)$ is the temporal Fourier transform of $f_l(t)$.

Because our derivation involves repeated differentiations and integrations, we employ the following notation:

$$f_l^{(n)}(t) \equiv \frac{d^n f_l(t)}{dt^n} \ . \tag{6.12}$$

For negative values of n, this notation implies integrating $f_l(t)$ n-times. In the frequency domain, the notation (6.12) translates into

$$F_l^{(n)}(\omega) \equiv (-i\omega)^n F_l(\omega) \ . \tag{6.13}$$

Next, we relate the total wavefield $u_l(r,t)$ to the spherical Bessel function of order 0 which makes it possible to evaluate the Fourier integral in equation (6.11) analytically. This derivation, found in the appendix, gives:

$$u_l(r,t) = c^l r^l \left(\frac{1}{r}\frac{d}{dr}\right)^l \left(\frac{f_l^{(-l)}(t+r/c) - f_l^{(-l)}(t-r/c)}{r}\right) \ . \tag{6.14}$$

This expression shows an explicit relationship between the total wavefield $u_l(r,t)$ for all values of r, and the incident wave, $f_l(t+r/c)/r$ at a great distance $r \to \infty$. Note that using the notation of equations (6.12)-(6.13), the incoming wave is integrated l times in the factor $f_l^{(-l)}(t \pm r/c)$, and that the differential operator $(1/r)(d/dr)$ acts l times as well. The term $f_l^{(-l)}(t+r/c)$ is the wave that converges on the focal point, while $f_l^{(-l)}(t-r/c)$ gives the outgoing wave that radiates from the focus after the incoming waves has passed through that point. The incident wave $f_l(t+r/c)$ and the outgoing wave $f_l(t-r/c)$ have opposite sign because the focus is a caustic in two angular directions, hence the Maslow index increases by two, which corresponds to a sign change [49].

We now demonstrate how we can use the expression for the wavefield near the focal point to demonstrate that improved temporal focusing leads to improved spatial focusing. The spatial focus $R_l(r)$ is defined as the wavefield at time $t = 0$. It follows from expression (6.14) that the spatial focus is given by:

$$R_l(r) \equiv u_l(r, t=0) = c^l r^l \left(\frac{1}{r}\frac{d}{dr}\right)^l \left(\frac{f_l^{(-l)}(r/c) - f_l^{(-l)}(-r/c)}{r}\right) \ . \tag{6.15}$$

This expression gives the spatial focus in terms of the incoming wave.

One might be tempted to define the temporal focus as $u_l(r=0,t)$. This field, according to expression (6.9), is proportional to $j_l(kr)$ in the frequency domain. The zeroth order Bessel function $j_0(kr)$ is nonzero for $r=0$, but $j_l(kr=0)=0$ for $l \geq 1$ [27]. This means that for $l \geq 1$, the wavefield vanishes at the focal point. Physically, this is due to the fact that for $l \geq 1$, the focal point ($r=0$) is located at the intersection of nodal lines. Since $U_l(r=0,t)$ vanishes at $r=0$ for $l \geq 1$, this quantity is not a useful diagnostic of the temporal focus. To remedy this, we define the temporal focus instead as

$$T_l(t) \equiv \frac{d^l}{dr^l} u_l(r=0,t) \; . \tag{6.16}$$

As shown in the appendix, the l-th derivative of $j_l(kr)$ is finite and nonzero for $r=0$. We derive in the appendix the following relation between the temporal focus and the incoming waves,

$$T_l(t) = \frac{2b_l}{c^{l+1}} f_l^{(l+1)}(t) \; , \tag{6.17}$$

where b_l is given by

$$b_l = \frac{2^l (l!)^2}{(2l+1)!}. \tag{6.18}$$

Specifically,

$$b_0 = 1 \;\; , \;\; b_1 = 1/3 \;\; , \;\; b_2 = 2/15.$$

According to equation (6.17), the temporal focus thus is proportional to the $(l+1)$-th time derivative of the incoming wave. Of these $(l+1)$ derivatives, given by equation (6.17), l are due to the derivatives in definition (6.16). One time derivate is due to the fact that (6.14) contains the combination $\left(f_l(t+r/c) - f_l(t-r/c)\right)/r$. Using a Taylor expansion and taking the limit $r \to 0$, gives

$$\lim_{r\to 0} \frac{f_l(t+r/c) - f_l(t-r/c)}{r} = \lim_{r\to 0} \frac{2(r/c) f_l^{'}(t)}{r} = \frac{2}{c} f_l^{'}(t).$$

This explains an additional time derivative in expression (6.17).

6.3 Spatial and temporal focus for each angular component

The spatial and temporal focus defined by expressions (6.15) and (6.17) both relate to the incoming waves and can be combined to explicitly relate the spatial and temporal focus:

$$R_l(r) = \frac{c^{2l+1}}{2b_l} r^l \left(\frac{1}{r}\frac{d}{dr}\right)^l \left(\frac{T_l^{(-2l-1)}(r/c) - T_l^{(-2l-1)}(-r/c)}{r}\right) . \tag{6.19}$$

Equation (6.19) is the main result of the theory. Although the relation (6.19) between the spatial and temporal focus is complicated, it does show that good temporal focusing implies good spatial focusing. Good temporal focusing implies that $T_l(t)$ is strongly peaked near $t = 0$, i.e. that $T_l(t)$ only differs appreciably from zero for a small range of time values $-t_f < t < t_f$, where t_f is the half width of the temporal focus. Expression (6.19) implies that the spatial focus differs appreciably from zero for values of r that satisfy $0 \leq r < ct_f$ (radius is always positive). A good temporal focus (small t_f) thus implies a good spatial focus.

The spatial and temporal focus, and their relationship defined by equations (6.15), (6.17), and (6.19) all depend on the order l. In this section, we show the explicit forms of these expressions for the case $l = 0$, $l = 1$, and $l = 2$. These cases are relevant for an explosive source ($l = 0$), point force ($l = 1$) and double-couple source ($l = 2$) if the aperture would be perfect. For $l = 0$, equations (6.15), (6.17), and (6.19) become respectively,

$$R_0(r) = \left(\frac{f_0(r/c) - f_0(-r/c)}{r}\right) , \tag{6.20}$$

$$T_0(t) = \frac{2}{c} f_0^{(1)}(t) , \tag{6.21}$$

$$R_0(r) = \frac{c}{2}\left(\frac{T_0^{(-1)}(r/c) - T_0^{(-1)}(-r/c)}{r}\right) . \tag{6.22}$$

Equations (6.20),(6.21), and (6.22) are the same as shown in the previous derivation of [28] which dealt with an explosive source in an acoustic medium where the temporal focus is the time derivative of the incoming wave.

We now continue the derivation for $R(r)$ due to a point force ($l = 1$) and double-couple ($l = 2$). For $l = 1$, equations (6.15), (6.17), and (6.19) become respectively,

$$R_1(r) = \frac{1}{r}\left(f_1(r/c) + f_1(-r/c)\right) - \frac{c}{r^2}\left(f_1^{(-1)}(r/c) - f_1^{(-1)}(-r/c)\right) \ , \tag{6.23}$$

$$T_1(t) = \frac{3}{2c^2} f_1^{(2)}(t) \ , \tag{6.24}$$

$$R_1(r) = \frac{2c^2}{3}\frac{1}{r}\left(T_1^{(-2)}(r/c) + T_1^{(-2)}(-r/c)\right) - \frac{2c^3}{3}\frac{1}{r^2}\left(T_1^{(-3)}(r/c) - T_1^{(-3)}(-r/c)\right) \ . \tag{6.25}$$

It may appear that equation (6.23) is singular at $r = 0$. Even though each of the two terms in this expression diverge as $r \to 0$, the singularities cancel. This can be verified by writing $f_1(r/c) = a_0 + O(r)$. Integrating this once gives $f_1^{(-1)}(r/c) = a_0(r/c) + O(r^2)$. Inserting this into equation (6.23) gives

$$R_1(r) = \frac{1}{r}\left(2a_0 + O(r)\right) - \frac{c}{r^2}\left(2a_0(r/c) + O(r^2)\right) \ . \tag{6.26}$$

The terms proportional to a_0, which caused each of the individual terms in expression (6.23) to be singular, cancel out. The remainder of equation (6.26) is finite as $r \to 0$.

For $l = 2$, equations (6.15), (6.17), and (6.19) become respectively,

$$R_2(r) = \frac{1}{r}\left(f_2(r/c) - f_2(-r/c)\right) - \frac{3c}{r^2}\left(f_2^{(-1)}(r/c) + f_2^{(-1)}(-r/c)\right) + \frac{3c^2}{r^3}\left(f_2^{(-2)}(r/c) - f_2^{(-2)}(-r/c)\right) \ . \tag{6.27}$$

$$T_2(t) = \frac{4}{15c^3} f_2^{(3)}(t) \ , \tag{6.28}$$

$$R_2(r) = \frac{15c^3}{4}\frac{1}{r}\left(T_2^{(-3)}(r/c) - T_2^{(-3)}(-r/c)\right) - \frac{45c^4}{4}\frac{1}{r^2}\left(T_l^{(-4)}(r/c) + T_l^{(-4)}(-r/c)\right) + \frac{45c^5}{4}\frac{1}{r^3}\left(T_l^{(-5)}(r/c) - T_l^{(-5)}(-r/c)\right) \ . \tag{6.29}$$

The wavefields computed are finite at the focal point $r = 0$ when one refocuses either P or S-waves. In contrast, when P and S-waves are excited by a point force, the P-wave component and the S-wave component behave as $1/r^3$ as $r \to 0$, hence the P-wave and S-wave separately

have a non-integrable singularity at $r = 0$, while their sum has an $1/r$ singularity [50], which is integrable. The refocused wavefields don't display this behavior because these fields are source-free at $r = 0$, and therefore the wavefield is finite. Therefore, the P and S-waves can be refocused separately without causing singularities, and the treatment given here is applicable to P, SV, and SH waves separately.

The expressions above must be multiplied with the appropriate vector spherical harmonic (6.2)-(6.4) to obtain the full focused wavefield. For each wave type, a different spherical harmonic must be multiplied to characterize the wavefield. Additionally, in equations (6.2)-(6.4), the vector spherical harmonics are summed over the angular order l and degree m which captures the imprint of the source properties on each wave type. Therefore, each wave has its own dependence on the angles and on space and time.

If one were to use one component of the motion, such as the x-component, the source properties for the different wave types are superposed on each other. Since for a fixed source mechanism the radiation pattern of P and S waves are different, the focused wavefields do not provide clear information about the source mechanism. In order to avoid mixing of P- and S- radiated waves, one must decompose the wavefield using the divergence and curl in order to investigate the focus of each wave type (P and S) separately.

If one does not have a perfect aperture, a blurred focus will occur, and the focus can not be characterized by one angular degree l but by the superposition of different angular degrees l. This is important to describe the spatial focus achieved in our numerical modeling.

6.4 Numerical Example

We illustrate the theory with a numerical example. We use the velocity model shown in the top panel of Figure 6.1 to propagate the source wavefield to the receivers. The model consists of horizontally continuous layers whose P-wave velocities range from approximately 4.7 km/s to 5.9 km/s and S-wave velocities range from approximately 2.3 km/s to 2.9 km/s. In practice, one does not know the true velocity model. For this reason, we used the smoothed velocity model, shown in the bottom panel of Figure 6.1, for the back-propagation. The

velocity model is smoothed by using a two-dimensional triangle smoothing of the slowness with a smoothing radius of .185 km in the x and z directions [44]. This smoothed velocity model has the same mean slowness as the correct velocity model.

We use a horizontal point force located at $(x, z) = (0.51$ km, 2.68 km). The source is characterized by Ricker wavelet with dominant frequency of 100 Hz. There are 56 receivers distributed over 2 vertical boreholes in our model. The x-locations of the receiver boreholes are 0.74 km and 0.88 km respectively. The receivers range from a depth of 2.36 km to 2.86 km with a spacing of 18.5 m.

6.5 Horizontal Point Force

This section describes the numerical modeling that demonstrates that improved temporal focusing leads to improved spatial focusing for each wave type. We first model the wavefield due to a horizontal point force excitation at the source location. The horizontal and vertical displacements of the wavefield are then recorded at each receiver. Afterwards, we apply either time reversal or deconvolution to the recorded signals to generate the wavefields which are back-propagated.

We use the time reversed or deconvolved signals to excite waves that backpropagate through the smoothed velocity model, using the following forces acting at each of the receiver locations,

$$\vec{F}_{TimeReverse} = (U_x(-t), U_z(-t))), \tag{6.30}$$

$$\vec{F}_{Deconv} = (U_x^{Inverse}(t), U_z^{inverse}(t)) \ . \tag{6.31}$$

Here, $\vec{F}_{TimeReverse}$ and $\vec{F}_{Deconv}$ are the source functions for time reversal and deconvolution respectively, and $U_x(t)$ and $U_z(t)$ are the recorded signals. The inverse signal of a time series $g(t)$ is defined as,

$$g^{inverse}(t) \star g(t) = \delta(t). \tag{6.32}$$

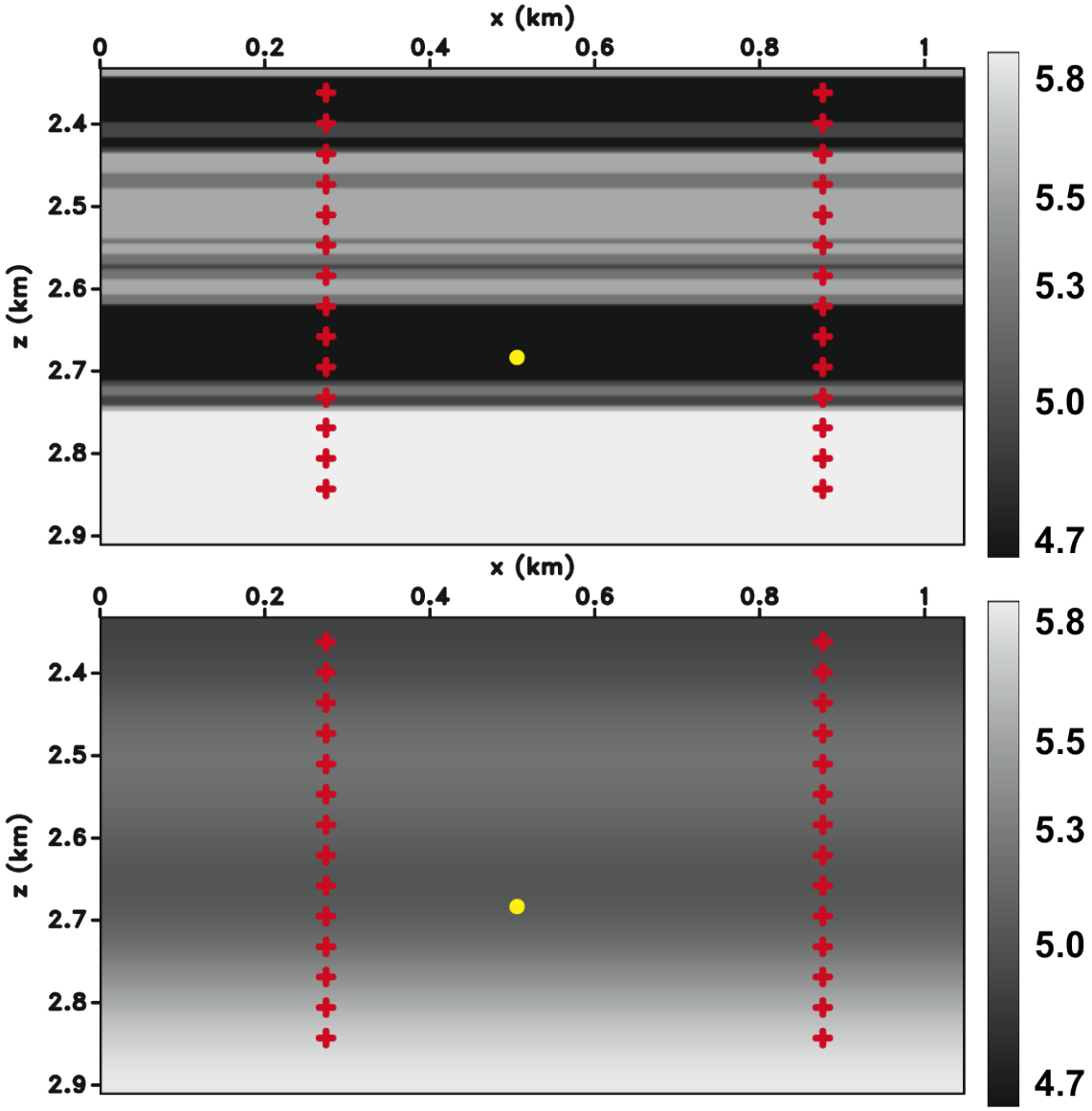

Figure 6.1: P-wave velocity models of the numerical experiment with units of km/s. Top panel indicates the correct velocity model and represents the velocity model used to propagate the source wavefield through the medium. Bottom panel indicates the smoothed velocity model with correct mean slowness. This model is used for back-propagation of the time reversed signal and optimized inverse signal. The plus symbols represent the receivers, the circular dot represents the source. The S-wave velocity was the same but had velocities values equal to half of the P-wave velocity.

where $\star$ denotes convolution. In order to solve for $g^{inverse}(t)$ and avoid instability for $g^{inverse}(\omega)$ when $g(\omega) = 0$, we have apply a water level regularization. Thus,

$$g^{inverse}(\omega) = \frac{1}{g(\omega)} \Rightarrow \frac{g^*(\omega)}{|g^*(\omega)|^2 + \epsilon}. \tag{6.33}$$

The derivation and explanation of these two methods are discussed in more detail by [47].

After backpropagation, the wavefield is decomposed into P and S components for a crucial reason. We demonstrated in the theory section that improved temporal focusing leads to improved spatial focusing for each wave type. We do not consider the focus for the vertical or horizontal displacements. Rather, we use the displacement components to calculate the P and S wavefields using divergence and curl, respectively. This allows us to retrieve the P and S waves that have backpropagated from the sources. For each wave type, our theory predicts that an improved temporal focusing leads to improved spatial focusing.

We first model the wavefield due to a horizontal point force excitation at the source location. The top panel of Figure 6.2 and Figure 6.3 show the P and S wavefields' radiation pattern just after the horizontal point force is emitted and represent a pure angular degree $l = 1$. In perfect source imaging, we would reconstruct these radiation patterns. However, our aperature is not perfect and we backpropagate through a smoother version of the velocity model. Thus, we do not expect to be able to reconstruct these radiation patterns perfectly.

In order to show that deconvolution generates an improved spatial focus, we first demonstrate that deconvolution enhances the temporal focus. Thus, we calculate the temporal focusing for the P and S component as a result of deconvolution (equation (6.31)) compared with time reversal (equation (6.30)). We defined the temporal focusing in equation (6.16) as the l-th derivative of the incoming wavefield. This is necessary because the wavefield is zero at our source location due to nodal lines. In order to demonstrate improved temporal focusing for a horizontal point force, we take the derivative of the P wavefield in the x-direction and the derivative of the S-wavefield in the z-direction because these derivatives are the radial derivatives perpendicular to the nodal lines for each wave type. We change the direction

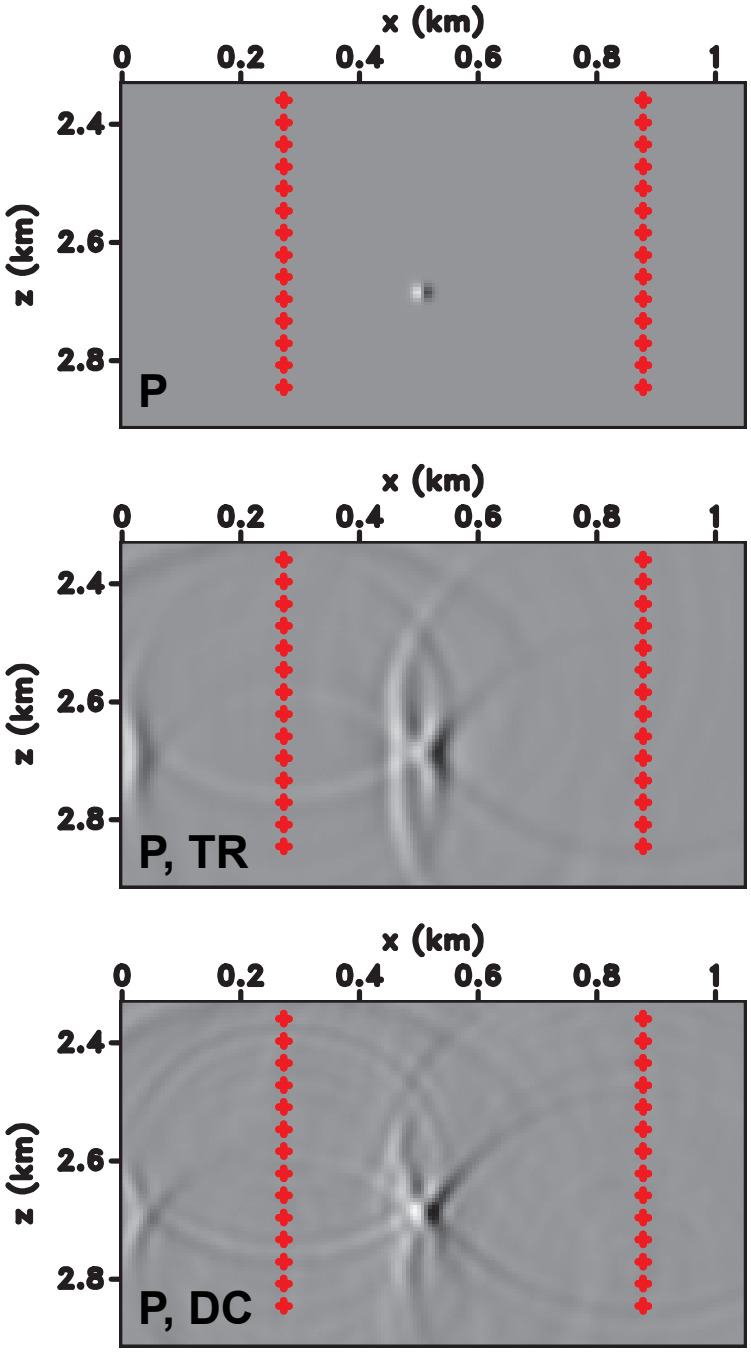

Figure 6.2: Decomposed P wavefield at time of focus due to horizontal point force. Top panel is P-wave just after the horizontal point force is emitted. Middle panel indicates the result of injecting the time reversed signal back into the smoothed velocity model from the receiver locations. Bottom panel shows result of injecting the inverse signal calculated using deconvolution back into the smoothed velocity model from the receiver locations.

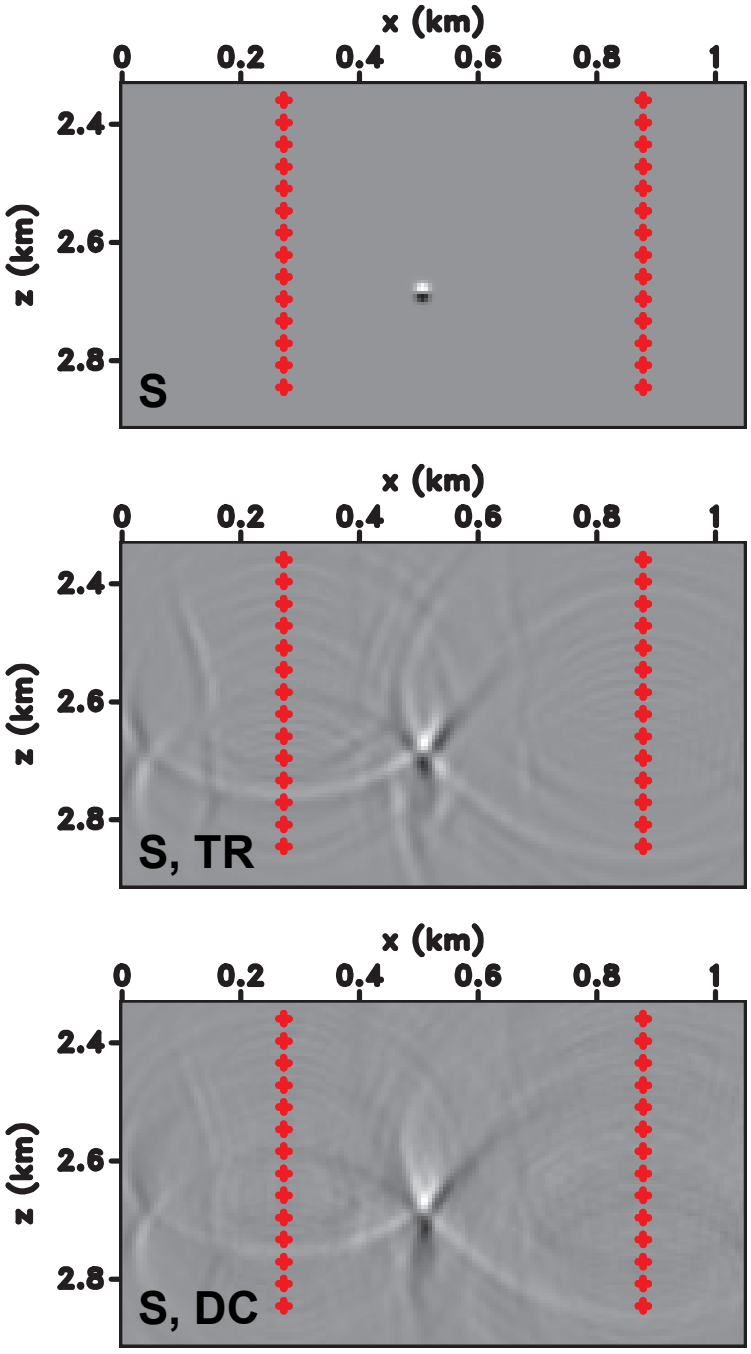

Figure 6.3: Decomposed S wavefield at time of focus due to horizontal point force. Top panel is S-wave just after the horizontal point force is emitted. Middle panel indicates the result of injecting the time reversed signal back into the smoothed velocity model from the receiver locations. Bottom panel shows result of injecting the inverse signal calculated using deconvolution back into the smoothed velocity model from the receiver locations.

of the derivative because the radiation pattern of the P-wave due to a horizontal point force is a dipole in the x-direction while the S-wave radiation has a dipole pattern oriented in the z-direction [48]. This is visible in the top panel of Figure 6.2 and Figure 6.3, which show the radiation patterns of the P and S wavefields just after the source has acted. We calculate the derivatives as defined above to show the temporal focus for the P and S wave at the source location. Comparing Figure 6.4(a) to (b), one can clearly note that deconvolution has significantly improved the temporal focusing compared to time reversal for the P-wave. In contrast, Figure 6.4(c) and (d) show that both time reversal and deconvolution produce a similar temporal focus for the S wave. Because improved temporal focusing implies better spatial focusing, see equation (6.26), one would expect to see an improved spatial focus improved for the P-wave using deconvolution compared to using time reversal. Additionally, we don't expect the S-wave's spatial focus to improve using deconvolution because the temporal focus did not improve.

After having demonstrated that deconvolution improved the temporal focusing for the P wave, we compare the spatial focus generated by deconvolution and time reversal for each wave type. The backpropagated wavefields at $t = 0$ for the two methods are shown in the middle and bottom panels of Figure 6.2 and Figure 6.3. The middle panel of Figure 6.2 represents the spatial focus of the P wave using time reversal whereas the bottom panel shows the spatial focus of the P wave using time-reversal. Figure 6.2 shows that deconvolution drastically improves the spatial focus compared to deconvolution. Figure 6.3 does not show a clear improvement of spatial focusing between time reversal (middle panel) and deconvolution (bottom panel) for the S component. This was expected due to deconvolution and time reversal producing similar temporal focuses for the S- wave.

The aperture, over which we record the data that we back-propagate, is not perfect. This causes the spatial focuses, created using time reversal and deconvolution shown in Figure 6.2 and Figure 6.3, to not be confined to one angular degree l because the spatial focuses are blurred in the z-direction. A perfect spatial focus would consist of only the

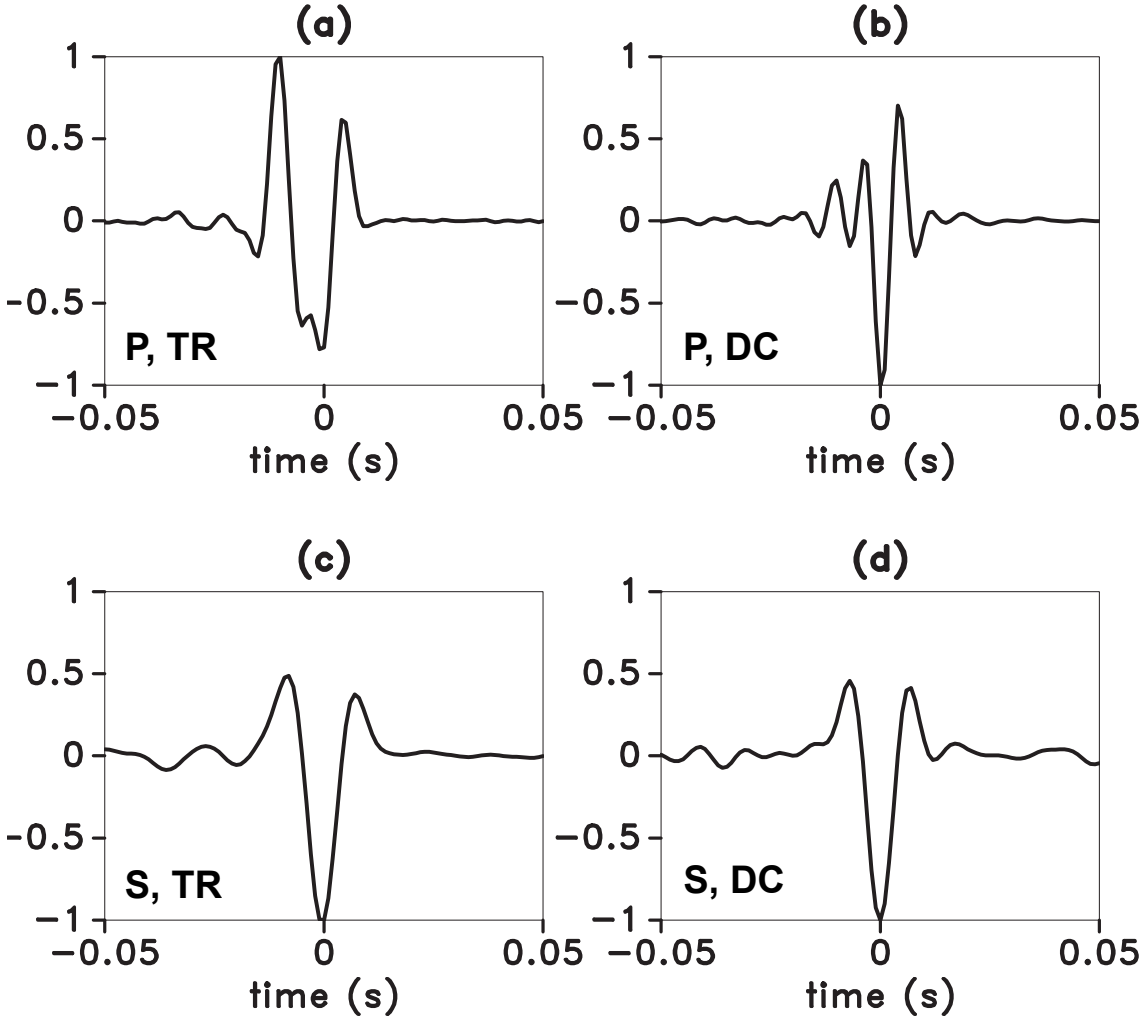

Figure 6.4: Temporal focused images due to a horizontal point force produced by back-propagating the calculated time reversed signals using time reversal and deconvolution for vertical borehole array. Part (a) and (b) are temporal focus of the P wave due to time reversal and deconvolution respectively. Part (c) and (d) are temporal focus of the S wave due to time reversal and deconvolution respectively.

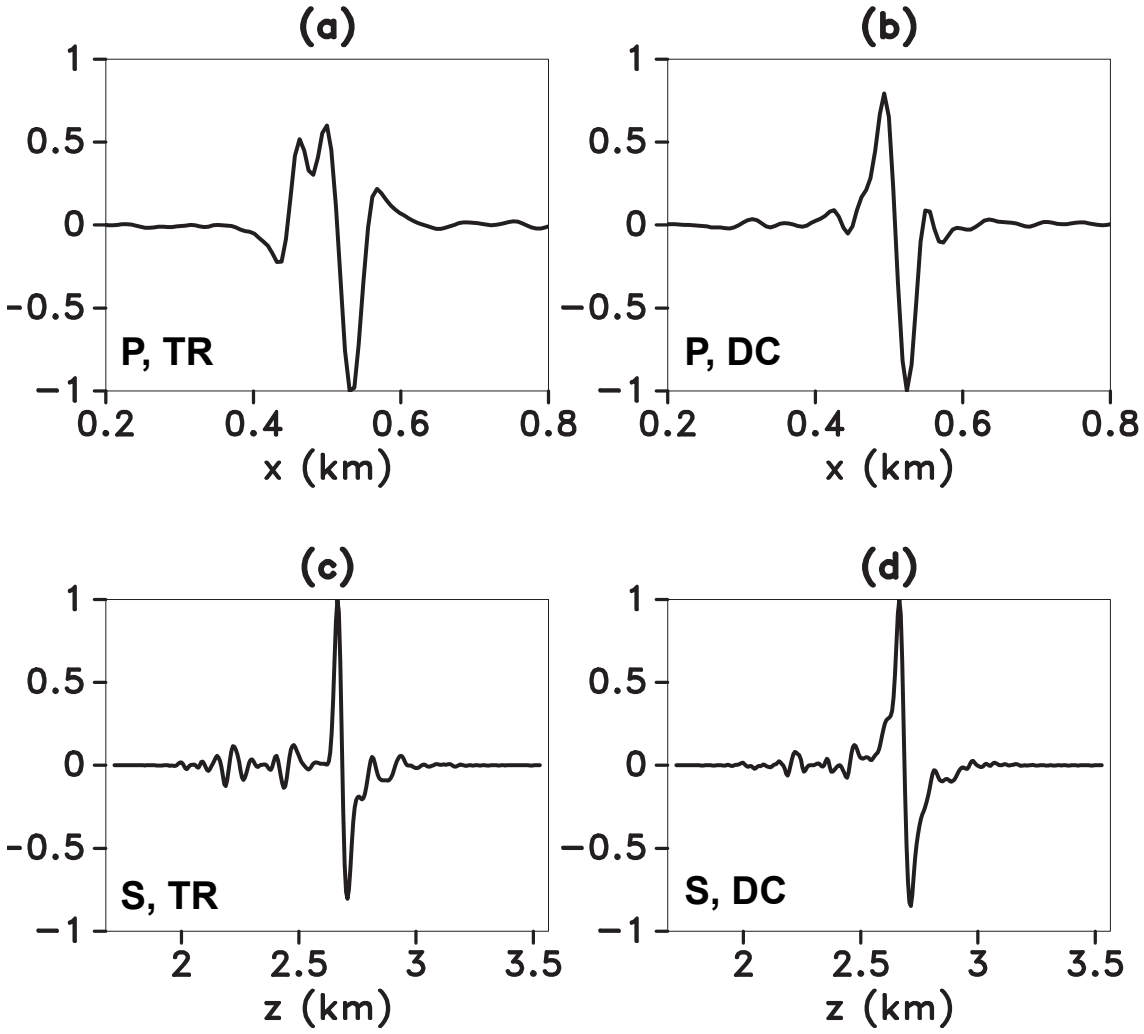

Figure 6.5: Spatial focused images due to a horizontal point force produced by back-propagating the calculated time reversed signals using time reversal and deconvolution. Part (a) and (b) are 1D slices of Figure 6.2 through depth 2.68 km. Part (c) and (d) are 1D slices of Figure 6.3 through x location .51km. Note the different scales used for the cross-section in the x and z direction.

$l = 1$ component. Figure 6.5(a)-(b) and (c)-(d) shows cross sections of the backpropagated wavefields in Figure 6.2 and Figure 6.3 in the x and z directions, respectively, so that it is easier to asses the improvements and comparisons between the two methods. Note that the scales of the horizontal axis for Figure 6.5(a)-(b) are different from Figure 6.5(c)-(d). Figure 6.5(a) demonstrates that time reversal is not able to create a well defined dipole focus in the x-direction which represents the radiation pattern of a P wave due to a horizontal point force. Figure 6.5(b) shows that deconvolution is able to reconstruct the dipole radiation pattern of the P wave due to a horizontal point force. Figure 6.5(c) and (d) demonstrate that there seems to be no significant difference between time reversal (c) and deconvolution (d) to reconstruct the S wave's focus.

Our numerical results have shown that deconvolution was able to improve the temporal focus for the P wave which led to an improved reconstruction of the P-wavefield's radiation pattern. However, deconvolution was not able to improve the temporal focus for the S-wave, due to a horizontal point force, which led to it also not improving the reconstruction of the S-wavefield's radiation pattern. This can be attributed to the fact that a nodal line for the S-wavefield's radiation pattern intersects the receiver array. Deconvolution will then apply a larger weight to the receivers near the nodal line in order to increase a weak recorded signal. This is unphysical because there is no information to be gained in these weak recorded waveforms near the nodal lines. These receivers are supposed to record no information about the source and should, therefore, not propagate any information back. However, it simultaneously demonstrates the robust nature of deconvolution. For the radiation pattern which has a nodal line intersecting the receiver array, deconvolution does not generate an inaccurate but rather a comparable reconstruction of the radiation pattern as time reversal.

We conclude that, for an elastic media without a perfect aperture and true velocity model, improved temporal focusing leads to improved spatial focusing. We have shown this both theoretically and numerically to be the case. Because deconvolution has the ability to improve the temporal focusing, one can improve the spatial focusing.

6.6 Conclusion

We have introduced deconvolution which improves the temporal focusing of microseismic events. We demonstrated theoretically and numerically that this improved temporal focusing leads to improved spatial focusing for each wave type in an elastic medium. This improved spatial focusing is beneficial for enhancing the focus of the elastic waves. The simplicity and robust nature of this method allows for a simple incorporation into existing reverse-time imaging methods. Additionally, the cost of deconvolution is minimal compared to running the finite difference modeling. Therefore, it can be added as a preprocessing step without significant additive cost.

CHAPTER 7

CONCLUSION

We have introduced a simple and robust method for determining the optimal signal for backpropagation such that one achieves an improved temporal focus at the source location. In Chapter 2, we show DC being used in a TR experiment in order to maximally compress the focus into an approximate delta function (with limited bandwidth) in both time and space or for optimal signal reconstruction. We explained theoretically why improved temporal focusing would lead to improved spatial focusing for an acoustic case. However, our experimental study comparing DC to TR also showed that, while temporal and spatial focusing have been enhanced with DC, there is a cost of a reduced maximum achieved amplitude. One might imagine the DC signal as a signal comprised of two components: one component allows for the focus of energy at the appropriate time and place, and another component simultaneously cancels noise at all other times and locations. Therefore, the focus generated using DC is cleaner and more impulse-like but not as strong because some of the energy is used to suppress the sidelobes.

Our previous experiments placed the source and receiver on the surface of our object. We wanted to do another experiment with the source within the specimen. The experiment was designed to recreate a scenario where a source event might occur within your object. We showed in Chapter 3 that for an experimental set up which had a receiver on the surface of the object and the sources embedded, one would still get a dramatically improved focus using DC. Due to the simplicity, low cost, and robust nature of this method, one could easily implement this technique into pre-existing workflows. This method may then be used to characterize the medium through use of virtual sources, repeated backpropagation or backpropagating with different source-function foci.

One of the main benefits of TR is its robust character. Therefore, we wanted to test the robust nature of DC in chapter 4 by studying the effect of of changing the stabilization constant γ used in the deconvolution and the impact multiple sources has upon deconvolutions' focusing abilities. This experiment used the same specimen as in our Chapter 3 study. However, this time we emitted all three embedded sources within the specimen. Additionally, we repeated our back propagation multiple times in order to record the focus for different deconvolved signals using a varying γ. We showed with this study that deconvolution was indeed robust, as one would still get a focus even with different γ values. Additionally, we also showed theoretically and experimentally why deconvolution would still work for multiple sources and may even have a significant improvement over time reversal.

Once the experimental studies were complete, we considered how the DC method might improve the ability to locate microseismic events. In Chapter 5, we compared DC to TR for an acoustic scenario where the wavefield is sampled sparsely, noise is present, and the velocity model is a smoothed version of the correct model. We demonstrated that DC is able to improve the spatial focus at the event location by improving the temporal focus. Due to the minimal cost of deconvolution compared to running the finite difference model, DC can be added as a pre-processing step without significant additional cost.

We were challenged by our reviewers to investigate the results of locating a microseismic event for an elastic case. This led us to Chapter 6 where we demonstrated theoretically and numerically that improved temporal focusing leads to improved spatial focusing for each wave type (P and S) in an elastic medium. It is important to note that one would not get an improved spatial focus if one looked at the vertical and horizontal displacement. One has to decompose the wavefield into P and S components in order for the theory of improved temporal focusing leading to improved spatial focusing to hold. We demonstrated this by showing the significant improvement achieved in reconstructing the radiation pattern due to a horizontal point force using DC instead of TR.

For future work, it would be beneficial to get a real data set of a microseismic survey, preferably both P and S data, and compare TR to DC. As stated previously, TR is already used in reverse time imaging to locate microseismic events. It would be worthwhile to apply DC to a pre-existing code, which processes real data, in order to compare the two methods.

REFERENCES CITED

[1] A. Parvulescu and C Clay. Reproducibility of signal transmission in the ocean. *Radio Elec. Eng.*, 29:223–228, 1965.

[2] M. Fink. Time reversed acoustics. *Physics Today*, 50(3):34–40, 1997.

[3] B. Anderson, M. Griffa, C. Larmat, T.J. Ulrich, and P.A. Johnson. Reproducibility of signal transmission in the ocean. *Acoustics Today*, 4:5–16, 2008.

[4] C.S. Larmat, R.A. Guyer, and P.A. Johnson. Time-reversal methods in geophysics. *Physics Today*, 63(8):31–35, 2010.

[5] P.M. Duncan. Is there a future for passive seismic? *First Break*, 23:111–115, 2005.

[6] M. Kendall, Shawn Maxwell, Gillian Foulger, Leo Eisner, and Zachary Lawrence. Special Section Microseismicity : Beyond dots in a box Introduction. *Geophysics*, 76(6):WC1–WC33, 2011.

[7] G.R. Foulger and Bruce R Julian. Earthquakes and errors: Methods for industrial applications. *Geophysics*, 76(6):WC5–WC15, 2012.

[8] M. Tanter, J.-L. Thomas, and M. Fink. Time reversal and the inverse filter. *J. Acoust. Soc. Am.*, 108:223–234, 2000.

[9] M. Tanter, J.-F. Aubry, J. Gerber, J.-L. Thomas, and M. Fink. Optimal focusing by spatio-temporal filter. I. Basic principles. *J. Acoust. Soc. Am.*, 110:37–47, 2001.

[10] G. Montaldo, M. Tanter, and M. Fink. Real time inverse filter focusing through iterative time reversal. *J. Acoust. Soc. Am.*, 115:768–775, 2004.

[11] F. Vignon, J.-F. Aubry, A. Saez, M. Tanter, D. Cassereau, G. Montaldo, and M. Fink. The Stokes relations linking time reversal and the inverse filter. *J. Acoust. Soc. Am.*, 119:1335–1346, 2006.

[12] T. Gallot, S. Catheline, P. Roux, and M. Campillo. A passive inverse filter for Green's function retrieval. *J. Acoust. Soc. Am.*, 131:EL21–EL27, 2011.

[13] V. Bertaix, Julien Garson, Nicolas Quieffin, Stefan Catheline, Julien Derosny, and Mathias Fink. Time-reversal breaking of acoustic waves in a cavity. *American Journal of Physics*, 72(10):1308–1311, 2004. ISSN 00029505. doi: 10.1119/1.1773577.

[14] P. Roux and M Fink. Time reversal in a waveguide: study of the temporal and spatial focusing. *J. Acoust. Soc. Am.*, 107:2418–2429, May 2000. ISSN 1520-8524.

[15] J.-F. Aubry, M. Tanter, J. Gerber, J.-L. Thomas, and M. Fink. Optimal focusing by spatio-temporal filter. II. Experiments. Application to focusing through absorbing and reverberating media. *J. Acoust. Soc. Am.*, 110:48–58, 2001.

[16] B. Lars G. Jonsson, Mats Gustafsson, Vaughan H. Weston, and Maarten V. de Hoop. Retrofocusing of acoustic wave fields by iterated time reversal. *SIAM J. Appl. Math.*, 64(6):1954–1986, 2004. ISSN 00361399.

[17] R. Daniels and R. Heath. Improving on time reversal with MISO precoding. In *Procedings of the Eighth International Symposium of Wireless Personal Communications Conference*, Aalborg, Danmark, 2005.

[18] R.C. Qiu, C. Zhou, N. Guo, and J.Q. Zhang. Time reversal with MISO for ultrawideband communications: experimental results. *IEEE Antennas and Wireless Propagation Lett.*, 5:1–5, 2006.

[19] P. Blomgren, P. Kyritsi, A. Kim, and G. Papanicolaou. Spatial focusing and intersymbol interference on multiple-input-single-output time reversal communication systems. *IEEE J. Oceanic Eng.*, 33:341–355, 2008.

[20] C. Zhou, N. Guo, and R.C. Qiu. Experimental results on multiple-input single-outpot (MISO) time reversal for UWB stystems in an office environment. In *MILCOM'06 proceedings of the 2006 IEEE conference on military comunications*, pages 1299–1304, Piscataway, NJ, 2006. IEEE Press.

[21] C. Zhou and R.C. Qiu. Spatial focusing of time-reversed UWB electromagnetic waves in a hallway enviroment:. In *Proceedings of the Thirty Eighth symposium on System Theory*, pages 318 – 322, 2006. doi: 10.1109/SSST.2006.1619051.

[22] F. Ciampa and M. Meo. Acoustic emission localization in complex dissipative anisotropic structures using a one channel reciprocal time reversal method. *J. Acoust. Soc. Am.*, 130:168–175, 2011.

[23] M. Meo and F. Ciampa. Impact detection in anisotropic materials using a time reversal approach. *Struct. Health Monitor.*, 11:43–49, 2012.

[24] R.W. Clayton and Ralph A. Wiggins. Source shape estimation and deconvolution of teleseismic bodywaves. *Geophys. J. Royal Astron. Soc.*, 47:151–177, 1976.

[25] B. Anderson, T.J. Ulrich, and P.-Y. Le Bas. Comparison and visualization of the focusing wave fields of various time reversal techniques in elastic media. *J. Acoust. Soc. Am.*, 134:EL527–EL533, 2013.

[26] B. Van Damme, K. Van Den Abeele, Y. Li, and O. Bou Matar. Time reversed acoustics techniques for elastic imaging in reverberant and nonreverberant media: An experimental study of the chaotic cavity transducer concept. *J. Appl. Phys.*, 95, 2011.

[27] G.B. Arfken and H.J. Weber. *Mathematical methods for physicists*. Harcourt, Amsterdam, 5th edition, 2001.

[28] T.J. Ulrich, Johannes Douma, Brian Anderson, and Roel Snieder. Improving spatio-temporal focusing and source reconstruction through deconvolution. *Wave Motion*, currently under review, 2013.

[29] K. Wapenaar, Filippo Broggini, and Roel Snieder. Creating a virtual source inside a medium from reflection data: heuristic derivation and stationary-phase analysis. *Geophysical Journal International*, 190(2):1020–1024, August 2012. ISSN 0956540X. doi: 10.1111/j.1365-246X.2012.05551.x.

[30] J. Behura and Roel Snieder. Virtual Real Source: Source signature estimation using seismic interferometry. *Geophysics*, 78(5):Q57–Q68, September 2013. ISSN 0016-8033. doi: 10.1190/geo2013-0069.1.

[31] K. Mehta, Jon L. Sheiman, Roel Snieder, and Rodney Calvert. Strengthening the virtual-source method for time-lapse monitoring. *Geophysics*, 73(3):S73–S80, May 2008. ISSN 0016-8033. doi: 10.1190/1.2894468.

[32] R. Snieder, Jon Sheiman, and Rodney Calvert. Equivalence of the virtual-source method and wave-field deconvolution in seismic interferometry. *Physical Review E*, 73(6):066620, June 2006. ISSN 1539-3755. doi: 10.1103/PhysRevE.73.066620.

[33] K. Mehta, Roel Snieder, Rodney Calvert, and Jon Sheiman. Acquisition geometry requirements for generating virtual-source data. *The Leading Edge*, May:620–629, 2008.

[34] J.C. Bancroft, Joe Wong, and Lejia Han. Sensitivity measurements for locating microseismic events. *CSEG Recorder*, (February):28–37, 2010.

[35] S. Bose, H Valero, Q Liu, R G Shenoy, and A Ounadjela. An Automatic Procedure to Detect Microseismic Events Embedded in High Noise. *SEG Technical Program Expanded Abstracts*, pages 1537–1541, 2009.

[36] K. Hayles, Robert L Horine, Steve Checkles, J P Blangy, and Hess Corporation. Comparison of microseismic results from the Bakken Formation processed by three different companies: Integration with surface seismic and pumping data. *SEG Technical Program Expanded Abstracts*, pages 1468–1472, 2011.

[37] J. Kummerow. Using the value of the crosscorrelation coefficient to locate microseismic events. *Geophysics*, 75(4):MA47–MA52, 2010.

[38] F. Song, H Sadi Kuleli, M Nafi Toksöz, Erkan Ay, and Haijiang Zhang. An improved method for hydrofracture-induced microseismic event detection and phase picking. *Geophysics*, 75(6):A47–A52, 2010.

[39] B. Artman, Igor Podladtchikov, and Ben Witten. Source location using time-reverse imaging. *Geophysical Prospecting*, 58:861–873, 2010. doi: 10.1111/j.1365-2478.2010.00911.x.

[40] R. Lu, N. Toksoz, and M.E. Willis. Locating Microseismic Events with Time Reversed Acoustics: A Synthetic Case Study. *SEG Technical Program Expanded Abstracts*, pages 1342–1346, 2008.

[41] R. Lu. Time Reversed Acoustics and Applications to Earthquake Location and Salt Dome Flank Imaging. *Massachusetts Institute of Technology. Earth Resources Laboratory*, 2008.

[42] B. Steiner, Erik H. Saenger, and Stefan M. Schmalholz. Time reverse modeling of low-frequency microtremors: Application to hydrocarbon reservoir localization. *Geophysical Research Letters*, 35(3):L03307, February 2008. ISSN 0094-8276. doi: 10.1029/2007GL032097.

[43] A. Parvulescu. Signal detection in a multipath medium by M.E.S.S. processing. *J. Acoust. Soc. Am.*, 33:1674–1674, 1961.

[44] S. Fomel. Shaping regularization in geophysical-estimation problems. *Geophysics*, 72 (2):R29–R36, 2007.

[45] G. McMechan, J.H. Luetgert, and W. Mooney. Imaging of earthquake sources in Long Valley Caldera, California, 1983. *Bull. Seismol. Soc. Am.*, 75:1005–1020, 1985.

[46] C. Larmat, J.P. Montagner, M. Fink, Y. Capdeville, A. Tourin, and E. Clévédé. Time-reversal imaging of seismic sources and application to the great Sumatra eartquake. *Geophys. Res. Lett.*, 33:L19312, doi:10.1029/2006GL02636, 2006.

[47] J. Douma, Roel Snieder, Ashley Fish, Paul Sava, and Wave Phenomena. Locating a microseismic event using deconvolution. *Proceedings of the 83rd Annual International Meeting, Society of Exploration Geophysicists.*, pages 2206–2211, 2013.

[48] K. Aki and P.G. Richards. *Quantitative Seismology.* Univ. Science Books, Sausalito, second edition, 2002.

[49] C. Chapman. *Fundamentals of seismic wave propagation.* Cambridge Univ. Press, Cambridge, UK, 2004.

[50] A. Wu, R.S.and Ben-Menahem. The elastodynamic near field. *Geophys. J.R. Astron. Soc.*, 81:609–622, 1985.

APPENDIX - IMPROVED TEMPORAL FOCUSING LEADS TO IMPROVED SPATIAL FOCUSING FOR AN ELASTIC MEDIUM

In this appendix, we derive an equation representing the spatial focusing in an elastic medium and demonstrate that has improved temporal focusing implies improved spatial focusing for each wave type.

We assume that the incoming wave $f_l(t)$ at angular degree l of expression (6.10) is given and first show how this function constrains the Fourier coefficient $A_l(\omega)$ in equation (6.9). The incoming wave is, in the frequency domain, given by

$$U_l^{inc}(r,\omega) = \frac{1}{2\pi}\int \frac{f_l(t+r/c)}{r} e^{i\omega t} dt = \frac{e^{-i\omega r/c}}{r}\frac{1}{2\pi}\int f_l(t) e^{i\omega t} dt = \frac{e^{-i\omega r/c}}{r} F_l(\omega)\ , \qquad \text{(A.1)}$$

where the replacement $t \to t - r/c$ is used in the second identity, and $F_l(\omega)$ is the incoming wave in the frequency domain. Because expressions (6.10) and (A.1) only hold in the limit $r \to \infty$, we proceed by analyzing equation (6.9) in the same limit where, according to equation (11.158) of [27], the spherical Bessel functions are given by

$$j_l(kr) = \frac{\sin(kr - l\pi/2)}{kr} = (-i)^{l+1}\,\frac{e^{ikr}}{2kr} + i^{l+1}\,\frac{e^{-ikr}}{2kr} \quad \text{as} \quad r \to \infty\ . \qquad \text{(A.2)}$$

The last term gives the incoming wave. Therefore, the incoming wave component of the spherical Bessel function at large distances r is given by $j_l^{inc}(kr) = i^{l+1}e^{-ikr}/2kr$ $(r \to \infty)$. Using this in expression (6.8) and equating it with equation (A.1) gives:

$$\frac{e^{-i\omega r/c}}{r} F_l(\omega) = i^{l+1}\,\frac{e^{-i\omega r/c}}{2kr} A_l(\omega) \quad \text{as} \quad r \to \infty\ . \qquad \text{(A.3)}$$

The r-dependence is the same on the left hand side and the right hand side of this equation. Equation (A.3) can be solved to give $A_l(\omega) = (-i)^{l+1}(2\omega/c)F_l(\omega)$. Inserting this into expression (6.9) leads to equation (6.11). This expression relates the total wavefield to the Fourier transform of the incoming wavefield. Note that this expression is valid for all values of r. The limit $r \to \infty$ was only used to relate $A_l(\omega)$ to the incoming wave.

The factor $(-i\omega)$ corresponds in the time domain to differentiation. In the following, we will apply repeated differentiations and integrations. For this reason we employ the notation shown in equations (6.12) and (6.13). Note that a negative value of n corresponds to an integration. With this notation, expression (6.11) can be written as

$$u_l(r,t) = (-i)^l \, \frac{2}{c} \int F_l^{(1)}(\omega) j_l(kr) e^{-i\omega t} d\omega \; . \tag{A.4}$$

The total wavefield (A.4) can also be related to the incoming wave in the time domain. In order to derive this, we use expression (11.165) of [27] to express the spherical Bessel function of order l into the spherical Bessel function of order 0: $j_l(x) = (-x)^l \left(\frac{1}{x} \frac{d}{dx} \right)^l j_0(x)$, hence

$$j_l(kr) = (-1)^l \frac{r^l}{k^l} \left(\frac{1}{r} \frac{d}{dr} \right)^l j_0(kr) \; . \tag{A.5}$$

Using equation (A.4) and the relation $k = \omega/c$ in equation (A.5) gives

$$u_l(r,t) = 2 r^l c^{l-1} \left(\frac{1}{r} \frac{d}{dr} \right)^l \int \frac{F_l^{(1)}(\omega)}{(-i\omega)^l} j_0(kr) e^{-i\omega t} d\omega \; . \tag{A.6}$$

Because of definition (6.13), $F_l^{(-1)}(\omega)/(-i\omega)^l = F_l^{(1-l)}(\omega)$, and we can simplify equation (A.6) to

$$u_l(r,t) = 2 r^l c^{l-1} \left(\frac{1}{r} \frac{d}{dr} \right)^l \int F_l^{(1-l)}(\omega) j_0(kr) e^{-i\omega t} d\omega \; . \tag{A.7}$$

The reason we relate $u_l(r,t)$ to the spherical Bessel function of order 0 is that this allows us to carry out the Fourier transform analytically. In order to do this, we use expression (11.148) of [27]

$$j_0(kr) = \frac{\sin kr}{kr} = \frac{c}{2i\omega r} \left(e^{i\omega r/c} - e^{-i\omega r/c} \right) \; , \tag{A.8}$$

where we use $k = \omega/c$ in the last identity. Using this result, the integral in equation (A.7) becomes

$$\begin{aligned} \int F_l^{(1-l)}(\omega) j_0(kr) e^{-i\omega t} d\omega \; &= -\frac{c}{2r} \int F_l^{(-l)}(\omega) \left(e^{-i\omega(t-r/c)} - e^{-i\omega(t+r/c)} \right) d\omega \\ &= \frac{c}{2r} \Big(f_l^{(-l)}(t + r/c) - f_l^{(-l)}(t - r/c) \Big) \; , \end{aligned} \tag{A.9}$$

where expression (A.8) was used in the first identity. Inserting equation (A.9) into equation (A.7) gives equation (6.14). This expression gives an explicit relation between the total wavefield for all values of r and the incident wave at great distance.

In order to determine the temporal focus (6.16), we need to evaluate $d^l j_l(kr)/dr^l$. According to equation (11.144) of [27],

$$j_l(x) = \frac{2^l l!}{(2l+1)!} x^l + O(x^{l+2}) \quad \text{as} \quad x \to 0 \; . \tag{A.10}$$

Using that $(d/dr)^l r^l = l!$, we get

$$\lim_{r\to 0} \frac{d^l}{dr^l} j_l(kr) = b_l k^l = b_l \omega^l / c^l \; , \tag{A.11}$$

where b_l is given by equation (6.18). Combining equations (6.16), (A.4), and (A.11) gives the following expression for the temporal focus

$$T_l(t) = \frac{2b_l}{c^{l+1}} \int (-i\omega)^l F_l^{(1)}(\omega) e^{-i\omega t} d\omega \; . \tag{A.12}$$

With the definition (6.11), this can be rewritten as

$$T_l(t) = \frac{2b_l}{c^{l+1}} \int F_l^{(l+1)}(\omega) e^{-i\omega t} d\omega \; . \tag{A.13}$$

Therefore, after taking the Fourier integral, we found a relationship between the temporal focus and the incoming wavefield.